Monthly Notices of the ROYAL ASTRONOMICAL SOCIETY

MNRAS **514,** 3113–3138 (2022) https://doi.org/10.1093/mnras/stac1019
Advance Access publication 2022 April 14

Apostle–Auriga: effects of different subgrid models on the baryon cycle around Milky Way-mass galaxies

Ashley J. Kelly [1]★ Adrian Jenkins [1] Alis Deason [1,2] Azadeh Fattahi [1] Robert J. J. Grand [3,4,5] Rüdiger Pakmor [3] Volker Springel [3] and Carlos S. Frenk[1]

[1]*Institute for Computational Cosmology, Department of Physics, Durham University, Durham DH1 3LE, UK*
[2]*Centre for Extragalactic Astronomy, Department of Physics, University of Durham, South Road, Durham DH1 3LE, UK*
[3]*Max-Planck-Institut für Astrophysik, Karl-Schwarzschild-Str 1, D-85748 Garching, Germany*
[4]*Instituto de Astrofísica de Canarias, Calle Vía Láctea s/n, E-38205 La Laguna, Tenerife, Spain*
[5]*Departamento de Astrofísica, Universidad de La Laguna, Av. del Astrofísico Francisco Sánchez s/n, E-38206 La Laguna, Tenerife, Spain*

Accepted 2022 March 15. Received 2022 March 14; in original form 2021 June 17

ABSTRACT

Modern hydrodynamical simulations reproduce many properties of the real Universe. These simulations model various physical processes, but many of these are included using 'subgrid models' due to resolution limits. Although different subgrid models have been successful in modelling the effects of supernovae (SNe) and active galactic nuclei (AGNs) feedback on galactic properties, it remains unclear if, and by how much, these differing implementations affect observable halo gas properties. In this work, we use 'zoom-in' cosmological initial conditions of two volumes selected to resemble the Local Group (LG) evolved with both the AURIGA and APOSTLE galaxy formation models. While the subgrid physics models in both simulations reproduce realistic stellar components of $L^\star$ galaxies, they exhibit different gas properties. Namely, AURIGA predicts that the Milky Way is almost baryonically closed, whereas APOSTLE suggests that only half of the expected baryons reside within the halo. Furthermore, APOSTLE predicts that this baryon deficiency extends to the LG ($r \leq 1$ Mpc). Some of the baryon deficiency in APOSTLE is due to SNe feedback at high redshift, which generates halo-wide outflows, with high covering fractions and radial velocities, which both eject baryons and significantly impede cosmic gas accretion. Conversely, in AURIGA, gas accretion into the halo appears to be almost unaffected by feedback. These differences appear to result from the different energy injection methods from feedback (both SNe and AGNs) to gas. Our results suggest that both quasar absorption lines and fast radio burst dispersion measures could constrain these two regimes with future observations.

Key words: galaxies: evolution – galaxies: formation – galaxies: haloes – galaxies: stellar content.

1 INTRODUCTION

In the Λ cold dark matter (CDM) cosmology, gravitationally bound dark matter structures grow by a combination of accretion of surrounding matter and mergers with smaller structures (Frenk et al. 1988). In this model, galaxies form by the cooling and condensation of gas at the centres of dark matter haloes (White & Rees 1978; White & Frenk 1991). Early tests of these models were carried out using cosmological simulations including dark matter and baryons (Katz & Gunn 1991; Navarro & Benz 1991; Katz, Hernquist & Weinberg 1992; Navarro & White 1993, 1994). These simulations were unable to reproduce important properties of real galaxies. In particular, they produced massive galactic discs that were too compact and rotated too fast (Navarro, Frenk & White 1995, 1997).

These early simulations did not include an efficient injection of energy from stellar winds and supernova (SN) explosions, a process now commonly referred to as 'feedback'. Feedback can efficiently suppress star formation by ejecting dense, star-forming gas, generating turbulence that disrupts star-forming regions and driving outflows that eject gas from the interstellar medium (ISM) in the form of a 'hot galactic wind' (Mathews & Baker 1971; Larson 1974). Efficient feedback prevents gas from cooling excessively at high redshift and prematurely turning into stars (White & Rees 1978; White & Frenk 1991; Pearce et al. 1999; Sommer-Larsen, Gelato & Vedel 1999; Thacker & Couchman 2001). Efficient feedback, from both SNe and active galactic nuclei (AGNs), is now a key ingredient of modern hydrodynamical simulations. These processes are crucial for reproducing observed galaxy properties such as the stellar mass function, the mass to size relation, and the mass to metallicity relation (e.g. Crain et al. 2009; Schaye et al. 2010, 2015; Le Brun et al. 2014; Vogelsberger et al. 2014a; Nelson et al. 2019).

While the inclusion of feedback in simulations is universal, there is no standard implementation of this process. The complexity of baryon physics, together with limited resolution, makes it impossible to include feedback *ab initio* from individual massive stars, SNe, or AGNs in representative cosmological simulations. Instead, simulations rely on 'subgrid' prescriptions of feedback, that is, physically motivated models whose parameters may be calibrated by reference to observational data. Thus, even though the physical

★ E-mail: a.j.kelly@durham.ac.uk

processes responsible for stellar winds, SNe, and AGNs feedback are not resolved, it is hoped that their effects on large scales can be faithfully reproduced.

Fundamentally, the SNe subgrid model describes how SNe energy from a single star particle, which typically represents a simple stellar population (SSP), is distributed to neighbouring gas elements. Energy can be injected into either a single gas resolution element, or into many, as kinetic (Navarro & White 1993; Dalla Vecchia & Schaye 2012) or thermal (Dalla Vecchia & Schaye 2012; Schaye et al. 2015) energy, or both (Springel & Hernquist 2003; Vogelsberger et al. 2014). There are subtleties within these different models such as the amount of energy available per mass of stars formed, thermal losses, the ratio of thermal to kinetic energy injection, the decoupling of hydrodynamics to disable cooling, and more. Similar considerations apply to AGNs feedback (see Smith, Sijacki & Shen 2018 for an in-depth review).

In modern simulations the free parameters of the SNe and AGN subgrid models are tuned to reproduce a selection of properties of real galaxies. Gas properties are rarely included in this calibration and are often taken as model predictions that can be compared with observational data. Large-scale gas properties such as cosmic accretion into haloes and on to galaxies have been studied extensively (e.g. Kereš et al. 2005; Brooks et al. 2009; Oppenheimer et al. 2010; Hafen et al. 2019; Hou, Lacey & Frenk 2019). These analyses illustrate how the injection of gas and metals by feedback complicates the baryon cycle within the circumgalactic medium (CGM) of galaxies, affecting gas inflow rates on to galaxies by both reducing the rate of first-time gaseous infall (van de Voort et al. 2011b; Nelson et al. 2015) and by recycling previously ejected winds (Oppenheimer et al. 2010). However, the sensitivity of these processes to the details of the subgrid model or the spatial scale at which they are significant is uncertain (van de Voort et al. 2011a).

Differences in hydrodynamical solvers introduce further uncertainty in the cosmological baryon cycle (Kereš et al. 2012; Sijacki et al. 2012; Torrey et al. 2012; Vogelsberger et al. 2012; Bird et al. 2013; Nelson et al. 2013). In general, it appears that hot gas in moving-mesh simulations cools more efficiently than in particle-based simulations; therefore, two simulations with the same subgrid model but different hydrodynamical solvers can have different gas properties. We do not investigate the effects of different hydrodynamical solvers in this work, although we consider the implications in light of our results. As we suspect, these differences turn out to be secondary to those introduced by the subgrid models (Hayward et al. 2014; Schaller et al. 2015; Hopkins et al. 2018).

In this paper, we focus on the effects of different implementations of SNe feedback on the Local Group baryon cycle. We compare the (untuned) emergent baryon cycle in the APOSTLE and AURIGA simulations of two Local Group-like volumes (Fattahi et al. 2016; Sawala et al. 2016). The two simulations use the same gravity solver and initial conditions (ICs) but have different subgrid galaxy formation models, with, in particular, very different approaches to SNe and AGNs feedback. The AURIGA simulations model SNe using hydrodynamically decoupled wind particles that are launched isotropically and, upon recoupling, inject both thermal and kinetic energy into the surrounding gas. In APOSTLE, SNe energy is injected as a 'thermal dump' which heats a small number of neighbouring gas elements to a pre-defined temperature. We also discuss the differences in the AGNs feedback between the two models; however, we find their effects are subdominant in our sample.

Despite the large differences in the subgrid model, which extends beyond the implementation of SNe feedback, both of these galaxy formation models produce galaxies at the present day that match many observed properties. Furthermore, both models have been demonstrated to give a good match to properties of the galaxy population as a whole. The APOSTLE model is a modified version of the EAGLE reference model (Crain et al. 2015; Schaye et al. 2015). However, it has 'weaker' AGN (due to slower black hole accretion and growth) and is used at an order-of-magnitude higher mass resolution than in the calibration runs (Crain et al. 2015). This difference in resolution is significant as the results of the EAGLE and similar models are resolution-dependent, as demonstrated in fig. 7 of Schaye et al. (2015). The AURIGA model has not been explicitly used in large cosmological simulations; however, it is based on the model used in the Illustris simulations (Vogelsberger et al. 2013, 2014; Torrey et al. 2014), and is similar to that in IllustrisTNG (Nelson et al. 2018) and FABLE (Henden et al. 2018).

The baryon cycle around galaxies, focussing on the CGM, has previously been studied in hydrodynamic simulations using particle tracking techniques similar to those in this work using both 'zoom' simulations (Nelson et al. 2013; Ford et al. 2014; Christensen et al. 2018; Sokołowska et al. 2018; Hafen et al. 2019, 2020; Suresh et al. 2019; Tollet et al. 2019) and large-volume cosmological simulations (Nelson et al. 2019; Borrow, Anglés-Alcázar & Davé 2020; Mitchell et al. 2020a; Mitchell, Schaye & Bower 2020b; Wright et al. 2020; Mitchell & Schaye 2022). In general, the different simulations agree that the CGM of the MW is dominated by cosmological gas accretion on first infall; however, the FIRE simulations (Hafen et al. 2019) predict much higher baryon fractions than EAGLE (Mitchell et al. 2020a; Wright et al. 2020) due to AGNs feedback in EAGLE. This paper builds on this foundation and compares the results between two different simulations, thus attempting to understand the results' model dependence.

This paper is structured as follows. In Section 2, we introduce our sample of simulated haloes and describe the stellar properties of the central galaxies, including morphology, surface density, and stellar-mass to halo-mass (SMHM) relation. In Section 3, we detail the SNe subgrid prescriptions and the tracer particles that facilitate comparisons. We also describe how we calculate the mock observables for ion column densities and the dispersion measure. We then present our results, starting with a baryon census around our Local Group analogues in Section 4, and a particle-by-particle analysis of the 'missing baryons' at $z = 0$ in Section 5. In Section 6, we attempt to understand how differences in the subgrid models lead to very different baryon cycles on scales up to ~ 1 Mpc. We present predicted observables in Section 7, and discuss the prospects of constraining the subgrid implementation of SNe feedback from current and future observational data sets. Finally, in Section 8 we discuss the implications of our results, including several caveats, and summarize our conclusions.

2 THE SAMPLE

We focus on ΛCDM hydrodynamical simulations of two Local Group-like volumes. Each is a zoom simulation of a region of radius 2–3 Mpc that contains a pair of large haloes with virial masses in the range 5×10^{11}–2.5×10^{12} $M_\odot$.[1] We refer to the four haloes, split across two volumes, as AP-*XX*-N*Y*, where *XX* = S5, V1 specifies which of the two volumes the halo is in, and *Y* = 1, 2 identifies

[1]We define the virial quantities, R_{200} and M_{200}, according to the spherical overdensity mass (Lacey & Cole 1994) of each halo centred around the most bound particle within the halo. R_{200} is the radius within which the mean enclosed density, $\Delta = 200$ times the critical density of the universe.

Table 1. Simulation parameters at $z = 0$. The columns are: (1) halo name in the form, AP-*XX*-*YY*-Apostle/Auriga, where *XX* and *YY* identify the volume and the halo, respectively; (2) halo virial mass; (3) halo radius; (4) baryon fraction within R_{200}; (5) stellar mass within 30 kpc; (6) the $\kappa_{\rm rot}$ rotation parameter; (7) radial scale length; (8) bulge effective radius; (9) Sersic index of the bulge; (10) black hole mass.

Halo name	Dark matter		Baryons						
	$\frac{M_{200}}{[10^{12}\,{\rm M}_\odot]}$	$\frac{R_{200}}{[{\rm kpc}]}$	$f_{\rm b}$	$\frac{M_*}{[10^{10}\,{\rm M}_\odot]}$	$\kappa_{\rm rot}$	$\frac{R_{\rm d}}{[{\rm kpc}]}$	$\frac{R_{\rm eff}}{[{\rm kpc}]}$	n	$\frac{M_{\rm BH}}{[{\rm M}_\odot]}$
AP-S5-N1-Apostle	0.91	199	0.53	2.03	0.58	3.31	1.00	1.02	$10^{6.37}$
AP-S5-N1-Auriga	0.99	205	0.89	5.89	0.66	1.87	0.55	1.04	$10^{8.11}$
AP-S5-N2-Apostle	0.79	190	0.64	1.60	0.54	3.21	0.91	1.06	$10^{6.27}$
AP-S5-N2-Auriga	0.80	191	0.88	3.95	0.64	2.15	0.49	1.07	$10^{7.59}$
AP-V1-N1-Apostle	1.64	242	0.82	4.49	0.58	3.93	1.05	0.99	$10^{6.81}$
AP-V1-N1-Auriga	1.64	242	0.86	10.51	0.59	7.62	0.68	0.73	$10^{7.96}$
AP-V1-N2-Apostle	1.02	207	0.59	1.62	0.26	3.51	1.21	1.06	$10^{6.38}$
AP-V1-N2-Auriga	1.12	213	0.99	3.77	0.68	3.74	0.89	0.92	$10^{7.36}$

the two primary haloes. AP-V1 and AP-S5 correspond to AP-1 and AP-11 in the original APOSTLE simulations described in Sawala et al. (2016) and Fattahi et al. (2016). The volumes were selected to match some of the dynamical constraints of the Local Group. The two primary haloes are required to have present-day physical separations of ≈800 kpc and radial velocities in the range 0–250 km s^{-1}. The volumes are also required to have no additional haloes of mass equal to, or greater than, the least massive of the pair within a radius 2.5 Mpc of the pair mid-point. More details about the selection criteria may be found in Fattahi et al. (2016).

The 'zoom-in' ICs were created using second-order Lagrangian perturbation theory implemented within IC_GEN (Jenkins 2010). These ICs have initial gas (dark matter) particle masses of $1.2(5.9) \times 10^5$ M$_\odot$, and maximum softening lengths of 307 pc. This resolution level corresponds exactly to the L2 resolution in Sawala et al. (2016) and Fattahi et al. (2016), and is similar to the level 4 resolution in Grand et al. (2017).

AP-*XX*-*YY*-Apostle are the APOSTLE simulations which were run using a highly modified version of the GADGET-3 code (Springel 2005). The fluid properties are calculated with the particle-based smoothed particle hydrodynamics (SPH) technique (Gingold & Monaghan 1977; Lucy 1977). The APOSTLE simulations adopted a pressure–entropy formulation of SPH (Hopkins 2013), with artificial viscosity and conduction switches (Price 2008; Cullen & Dehnen 2010) which, when combined, are known as ANARCHY (Schaye et al. 2015). This set-up is the same as that in the EAGLE simulations.

The AURIGA simulations, AP-*XX*-*YY*-Auriga, were performed with the magnetohydrodynamics code AREPO (Springel 2010). The gas is followed in an unstructured mesh constructed from a Voronoi tessellation of a set of mesh-generating points which then allow a finite-volume discretization of the magnetohydrodynamic equations. The mesh-generating points can move with the fluid flow. This moving mesh property reduces the flux between cells, thus reducing the advection errors that afflict fixed mesh codes. For a detailed description we refer the reader to Springel (2010) and Grand et al. (2017).

The AURIGA simulations follow the amplification of cosmic magnetic fields from a minute primordial seed field. The magnetic fields are dynamically coupled to the gas through magnetic pressure. Pillepich et al. (2017) demonstrate that the SMHM relation is sensitive to the inclusion of magnetic fields, particularly for haloes of $M_{200} \geq 10^{12}$ M$_\odot$. However, this is not important in this work as both galaxy formation models are calibrated to reproduce realistic $L^\star$ galaxies.

While the general method of calculating the physical fluid properties in the two simulations is different, there are some similarities. Both numerical schemes have the property that resolution follows mass, namely, high-density regions are resolved with more cells or particles. Also, both APOSTLE and AURIGA have the same method for calculating gravitational forces: a standard TreePM method (Springel 2005). This is a hybrid technique that uses a Fast Fourier Transform method for long-range forces, and a hierarchical octree algorithm for short-range forces, both with adaptive time-stepping.

The ICs are chosen to produce present-day Milky Way (MW) and M31 analogues. As both the AURIGA and APOSTLE simulations share exactly the same ICs, we expect several properties of the simulations to be similar. Specifically, the dark matter properties should be consistent in both simulations. Furthermore, as both simulations tune the subgrid models to recover real galaxy properties, we expect some stellar properties to be similar, but less so than the dark matter properties.

Dark matter haloes are identified using a Friends-of-Friends (FoF) algorithm (Davis et al. 1985). The constituent self-bound substructures (subhaloes) within an FoF group are identified using the SUBFIND algorithm applied to both dark matter and baryonic particles (Springel et al. 2001; Dolag et al. 2009).

Table 1 lists properties of the two primary haloes in both volumes. We see that the baryonic properties of the four haloes in the two simulations differ somewhat, with up to a factor of two difference in the stellar mass. We also tabulate the baryon fraction, $f_{\rm b}$, in each halo, which we define as the ratio of baryonic to total mass normalized by the mean cosmic baryon fraction, $\Omega_{\rm b}/\Omega_{\rm m} \sim 0.167$, within R_{200}. We find that the baryon fraction in the APOSTLE simulations is systematically lower than in their AURIGA counterparts. The virial properties of the haloes are all consistent, however, with small differences in virial mass and radius which are due to the different halo baryon fractions.

Fig. 1 shows a dark matter projection of the AP-S5 volume in both APOSTLE and AURIGA. A visual inspection shows that the dark matter distribution of the two haloes, and their local environment, is almost identical in the two simulations. There is some variation in the location of satellite galaxies and nearby dwarf galaxies; this is likely due to the different baryonic properties and the stochastic nature of *N*-body simulations.

In Fig. 2, we plot the SMHM relation for the four primary haloes in the two simulation volumes, APOSTLE and AURIGA, alongside the inferred relation from abundance matching (Behroozi, Wechsler & Conroy 2013). We also include several resolved lower mass

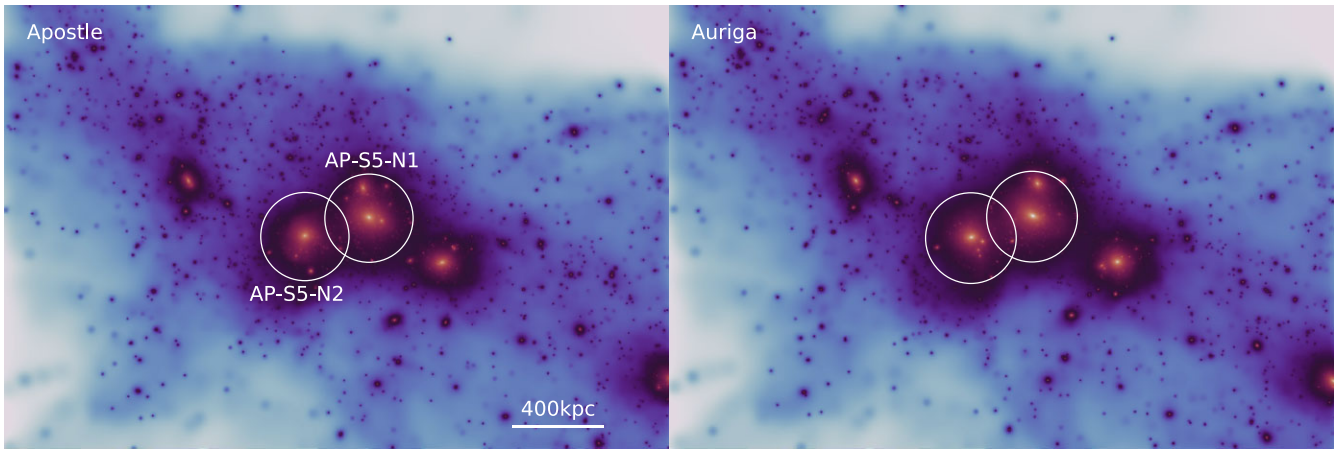

Figure 1. Present-day mass-weighted density projection of the dark matter for the AP-S5 volume in both APOSTLE (left) and AURIGA (right). The projected rectangle has dimensions of (3 × 2 × 3) Mpc in the *x*, *y*, and *z* directions, respectively, centred on the centre of the mass of the two primary haloes. The white circles illustrate R_{200} for these two haloes. The two main haloes do not overlap in 3D space but they do in this particular *x*-*y* 2D projection.

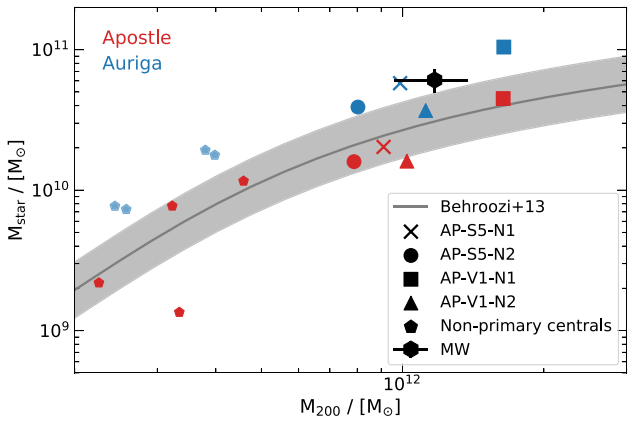

Figure 2. The SMHM relation in the APOSTLE (red) and AURIGA (blue) simulations. The four different symbols (cross, circle, square, and triangle) differentiate the four different primary haloes. The smaller blue and red pentagons show the SMHM relation for 'central' field galaxies in the APOSTLE and AURIGA simulations, respectively. The black solid line and grey shaded region are the results of Behroozi et al. (2013) with an estimated scatter of ±0.2 dex. We also show as a black hexagon with errorbars the estimate for the MW halo mass by Callingham et al. (2019) and of the stellar mass by Licquia & Newman (2015).

field 'central'[2] haloes from both APOSTLE and AURIGA to give an indication of the SMHM over a broader mass range. We define the stellar masses as the total stellar mass within an aperture of 30 kpc. The stellar masses of the AURIGA galaxies are consistently larger than those of the APOSTLE galaxies, at a given halo mass, over the entire range of halo masses. As both APOSTLE and AURIGA model the same volume, the differences are not due to sample variance. However, these are only single realizations of the model, and most galaxy formation models incorporate highly stochastic processes; thus rerunning these simulations may produce somewhat different results (Genel et al. 2019; Keller et al. 2019; Davies, Crain & Pontzen 2021).

Despite using a modified and higher resolution version of the EAGLE galaxy formation model, the four APOSTLE haloes in this work are similar to their EAGLE counterparts. The four APOSTLE haloes, which have a halo mass $\sim 10^{12}$ $M_\odot$, have a stellar mass range, $M_* \sim (1–5) \times 10^{10}$ $M_\odot$. This is in agreement with the EAGLE reference simulations which predict a range of $(0.5–5) \times 10^{10}$ $M_\odot$ (see fig. 7 of Matthee et al. 2017). The black hole mass of the four APOSTLE haloes is approximately a few $\sim 10^6$ $M_\odot$, which is very similar to those of the EAGLE reference simulation with the same stellar/halo mass (see fig. 10 of Schaye et al. 2015). However, the APOSTLE haloes in this study are considerably more baryon rich than those found in the EAGLE reference simulation. This predicts 15th and 85th percentiles for the halo baryon fraction of $f_b \sim 0.3–0.45$, for halo masses of $\sim 10^{12}$ $M_\odot$ (see fig. 1 of Kelly, Jenkins & Frenk 2021). The lowest baryon fraction of the APOSTLE haloes presented in Table 1 is $f_b = 0.53$. The reason for the larger baryon fraction in APOSTLE is likely twofold. First, the APOSTLE simulations use the 'ViscLo' subgrid physics parameters, which are identical to the EAGLE reference parameters except for a lower viscosity for the BH's subgrid accretion. Thus, the APOSTLE black holes will accrete at a lower rate than EAGLE black holes. Secondly, the EAGLE simulations were calibrated at a lower resolution. Using a similar model with higher mass resolution can make the stellar feedback more efficient which can reduce gas accretion on to the BH, stalling its growth and reducing AGNs feedback. Oppenheimer et al. (2020a) demonstrated that sudden black hole growth, and AGNs feedback, can reduce the baryon fraction around MW-mass haloes.

We also briefly analyse the stellar surface density profiles of the four primary haloes at the present day. We fit the surface density profiles with a combination of an exponential profile of scale radius, R_D, and a Sersic profile of the form $\exp(R/R_{eff})^n$ (Sérsic 1963). The values of the best-fitting parameters, R_D, R_{eff}, and n, are given in Table 1. The fit parameters of the models are consistent with the isolated MW-mass galaxies, the original AURIGA haloes, presented in Grand et al. (2017). Furthermore, the stellar surface density at the solar radius is a few times ~ 10 $M_\odot$ pc^{-2} in all of the haloes, which is consistent with estimates for the MW (Flynn et al. 2006). The surface density profiles, and the best-fitting models, can be seen in Fig. A1. The galaxy stellar surface density profiles are similar in most cases in the two simulations, albeit with a systematically higher surface density in the case of AURIGA.

We also calculate the κ_{rot} rotation parameter for each galaxy, a measure of the fraction of kinetic energy in organized rotation, which correlates with morphology (Sales et al. 2012). The quantity κ_{rot} is

[2] 'Central' refers to the most massive subhalo with an FoF (Davis et al. 1985) group.

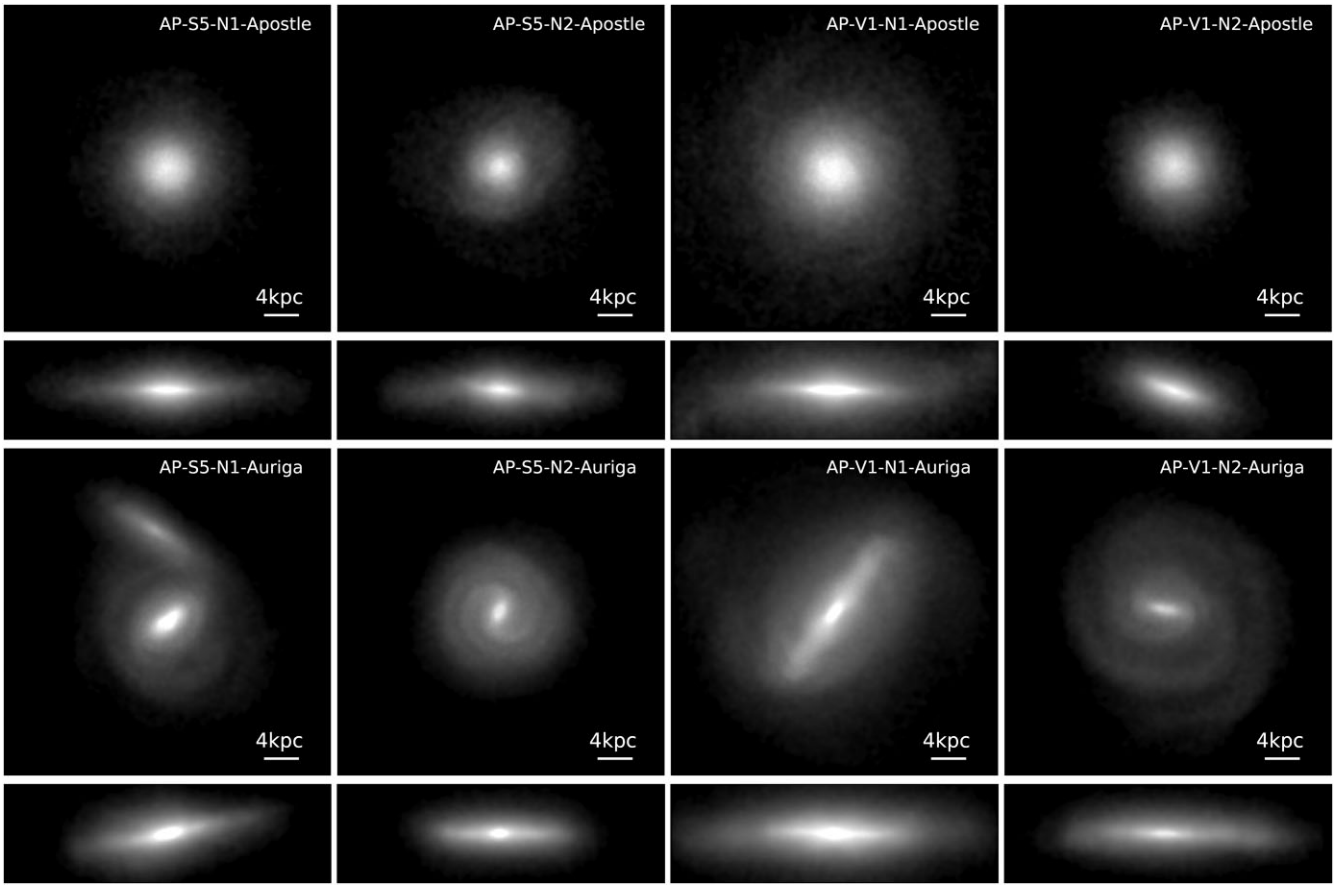

Figure 3. Mass-weighted face-on (top) and edge-on (bottom) projections of the stars in the four haloes in the APOSTLE and AURIGA simulations at $z = 0$.

defined such that $\kappa_{\rm rot} \approx 1$ for discs with perfect circular motions and $\kappa_{\rm rot} \approx 1/3$ for systems with an isotropic velocity dispersion. Thus, a large $\kappa_{\rm rot}$ indicates a disc galaxy, whereas a lower value indicates an elliptical galaxy. $\kappa_{\rm rot}$ requires a definition of the z-axis which we take to be the direction of the total angular momentum of all stars within 30 kpc of the centre of the galaxy. The large values of $\kappa_{\rm rot}$ in Table 1 are consistent with a visual inspection of Fig. 3, which shows face-on and edge-on stellar projections of the four primary haloes. In Fig. 3, we see that most of the galaxies appear to be 'discy' in projection, with the exception of AP-V1-N2-Ea, which has a low $\kappa_{\rm rot}$.

In general, the AURIGA simulations exhibit more recognizable morphological features, spiral arms, and distinct bar components (AP-S5-N2, AP-V1-N1, and AP-V1-N2). The APOSTLE simulations produce smoother looking discs, with little morphological evidence of either a bar or spiral arms. It is unclear what causes these morphological differences, but they could be due to different effective spatial resolutions in the two simulations. In SPH simulations, the smoothing length determines the spatial resolution, and the ratio of the smoothing length to the mean inter-particle separation is usually a free parameter taken to be ∼1.3 (Price 2012), whereas in moving mesh simulations, the cells have a spatial radius of ∼0.5 the mean cell separation. Thus, moving mesh simulations typically have a ∼1.3/0.5 ∼2.4 times better spatial resolution at the same mass resolution.[3]

[3]By the same mass resolution, we mean that the cell mass in a moving mesh simulation is equal to the particle mass in an SPH simulation, as in this work.

3 METHODS AND OBSERVABLES

3.1 Subgrid physics models

APOSTLE and AURIGA include prescriptions for subresolution baryonic processes such as star formation (Schaye & Dalla Vecchia 2008), metal enrichment (Wiersma et al. 2009b), black hole seeding and growth, AGNs feedback (Springel 2005; Booth & Schaye 2009; Rosas-Guevara et al. 2015), radiative cooling (Wiersma, Schaye & Smith 2009a), and feedback from stellar evolution (Dalla Vecchia & Schaye 2012). However, as previously noted, the implementations are rather different. In this section, we describe the qualitative differences in the SNe feedback prescriptions in the two models.

Traditionally, the energy from SN events occurring within the SSP represented by a star particle is injected into a large mass of local gas (Dalla Vecchia & Schaye 2008). If SNe energy from an SSP is injected over a mass of gas comparable to the initial stellar mass formed, the gas is heated to high temperatures, $T \geq 10^7$ K. However, when the same amount of energy is distributed over a much larger mass of gas, the temperature increase experienced by the gas is much lower. This lower post-SNe gas temperature results in a shorter cooling time. When the cooling time is significantly shorter than the sound-crossing time of the gas, energy injection from SNe is unable to drive a galactic wind efficiently (e.g. Dalla Vecchia & Schaye 2012).

In the APOSTLE simulations all the SNe energy from an SSP is injected in the form of thermal energy (Schaye et al. 2015). Rather than distributing the energy evenly over all of the neighbouring gas

particles, the energy is injected into a small number of neighbours *stochastically* (Dalla Vecchia & Schaye 2012). This method allows the energy per unit mass, which corresponds to the temperature change of a gas particle, to be defined. In these simulations each gas particle heated by SN feedback is always subject to the same temperature increase, $\Delta T_{\rm SN} = 10^{7.5}$ K.

The SNe feedback scheme in the AURIGA simulations consists of an initially decoupled wind whose main free parameters are the energy available per unit mass of SNII and the wind velocity. The wind velocity scales with the one-dimensional velocity dispersion of local dark matter particles. Qualitatively, SNe winds are modelled by 'wind particles' which are launched in an isotropic random direction carrying mass, energy, momentum, and metals. Upon launch, the wind particles are decoupled from hydrodynamic forces and experience only gravity. The wind particles can recouple either when they reach a region of low-density gas (5 per cent of the star-formation density threshold) or when they exceed a maximum travel time (0.025 of the Hubble time at launch). When the wind recouples, it deposits energy, momentum, and metals into the gas cells it intersects.

We do not describe the AGNs feedback models but detailed explanations of them can be found in Schaye et al. (2015) and Grand et al. (2017) for APOSTLE and AURIGA, respectively. The AGN model used in the APOSTLE simulations in this work differs from the EAGLE reference model in Schaye et al. (2015). Namely, in this work the AGN model uses a viscosity which is hundred times lower than the reference model; this reduces the accretion rate and growth of the black holes. This model is referred to as 'ViscLo' in Crain et al. (2015). In Section 8, we discuss the possible effects of the different AGN models on our results.

3.2 Tracer particles and particle matching

The quasi-Lagrangian technique of AREPO allows mass to advect between gas cells so each cell may not represent the same material over the course of the simulation. The AURIGA simulations, however, include Lagrangian Monte Carlo tracer particles (Genel et al. 2013; DeFelippis et al. 2017) which enable us to track the evolutionary history of individual gas mass elements in a way that allows direct comparison to SPH gas particles in APOSTLE. The Monte Carlo tracer particles have been shown to reproduce the density field in various tests, including cosmological simulations, accurately (Genel et al. 2013).

In AURIGA, a single tracer particle is attached to each gas cell at the beginning of the simulation. As the simulation proceeds, tracer particles can transfer across cell boundaries with a probability given by the ratio of the outward-moving mass flux across a face and the mass of the cell. This allows the tracer particles to emulate the evolution of a Lagrangian gas element. The tracer particles do not carry any physical properties. Instead, they inherit the properties of the baryonic element to which they are attached at any given time. The tracer particles introduce a Poisson noise due to their probabilistic evolution. However, as we use several million tracer particles, this noise is insignificant.

A combination of identical ICs and the tracer particles in AURIGA allows us to perform a detailed comparison between the two simulations on the scales of individual baryonic mass-elements. In the APOSTLE simulations, each dark matter particle in the ICs is assigned a gas particle at the start of the simulation. This represents the baryonic mass from the same Lagrangian region as the associated dark matter particle. Likewise, the dark matter particles within AURIGA are assigned tracer particles. Both the tracer particles in AURIGA and the gas particles in APOSTLE are assigned permanent, unique IDs dependent on their parent dark matter particle. The unique ID assigned to each particle facilitates direct comparison of the same baryonic mass elements between the two simulations.

3.3 Ion number densities

We calculate column densities of several ionized species following Wijers et al. (2019). The total number of ions, N_{X_i}, of each species in a given mass of gas is given by

$$N_{X_i} = \frac{m_X f_{X_i}}{m_Z}, \tag{1}$$

where m_X is the total mass of element X, f_{X_i} is the ionization fraction of the ith ion, m_Z is the mass of an atom of element X, and Z is the atomic number of the ionized element.

We calculate the ionization fraction of each species using the lookup tables of Hummels, Smith & Silvia (2017). These are computed under the assumption of collisional ionization equilibrium (CIE). They only consider radiation from the metagalactic UV background according to the model of Haardt & Madau (2012) in which the radiation field is only a function of redshift. The lookup tables are generated from a series of single-zone simulations with the photoionization code, CLOUDY (Ferland et al. 2013) and the method used for the 'grackle' chemistry and cooling library (Smith et al. 2016). The ion fractions are tabulated as a function of log temperature, log atomic hydrogen number density, and redshift.

In both APOSTLE and AURIGA the masses of some elements are tracked within the code; these are hydrogen, helium, carbon, nitrogen, oxygen, neon, magnesium, silicon, and iron. We calculate the number of species of each element from equation (1) with the total mass of each element as tracked by the code, and the calculated mass fraction of each species state. We can then make two-dimensional column density maps of each species by smoothing the contribution from each gas particle on to a 2D grid with a two-dimensional SPH smoothing kernel. We make these 2D maps by projecting through each of the x, y, and z axis. We then separate the 2D maps, which cover a region of (8×8) R_{200}, into 100 annuli with linearly spaced radii. In each annulus, we have many lines of sight through the halo. We then take the column density at radius, r, to be the median column density calculated within the annulus that encloses the radius, r, for all three projected maps. We choose to use the median as it is more representative of a single random line of sight through a halo in the real universe. However, the mean value, which is often significantly higher, is also of interest as observed values can be biased by the detection thresholds of instruments.

APOSTLE and AURIGA use different yield tables when calculating the fraction of different elements returned from SNIa to the ISM. These yield tables typically differ by < 20 per cent for the species considered in this work. However, these difference are negligible in the results presented in Section 7.1, which span many orders of magnitude. It is possible to normalize these yield fractions in post-processing, but we choose to use the simulation tracked quantities are they are self-consistent with the gas cooling.

3.4 The dispersion measure

Fast radio bursts (FRBs) are bright pulses of radio emission with periods of order milliseconds, typically originating from extragalactic sources (see review by Cordes & Chatterjee 2019). The first FRB, which was reported by Lorimer et al. (2007), was found in archival data from the 64 m Parkes radio telescope. By 2019, there were over 80 distinct FRB sources reported in the literature (see review by

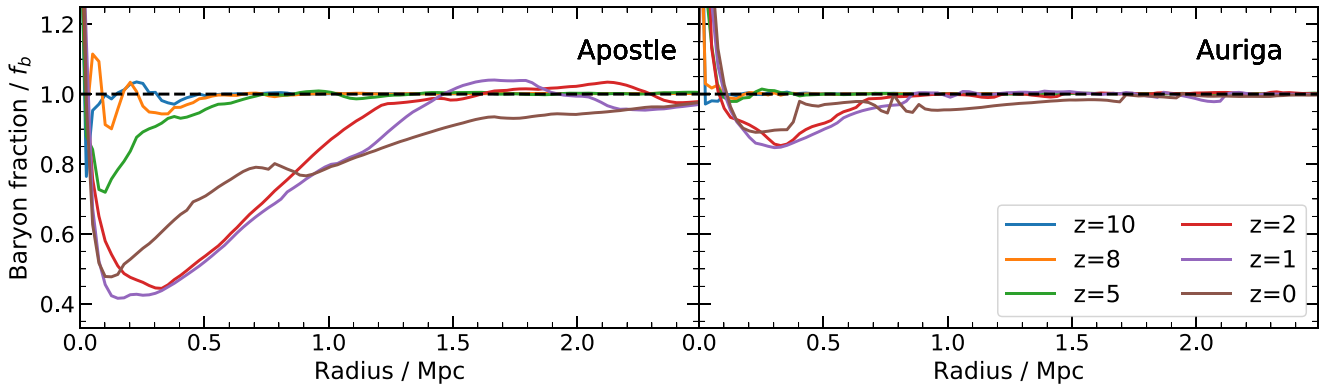

Figure 4. The baryon fraction within a sphere centred around the primary halo, AP-S5-N1, as a function of the sphere radius. The baryon fraction is calculated within 100 spheres with a linearly increasing radius in the range 0–2.5 Mpc (comoving). We repeat the process at six redshifts, $z = 0$, 1, 2, 5, 8, and 10, which are shown by the brown, purple, red, green, orange, and blue solid lines, respectively. The left-hand panel shows the results in APOSTLE and the right-hand panel in AURIGA. The baryon fraction is normalized by the mean baryonic-to-dark matter ratio, f_b, in the universe. The dashed black line indicates a baryonically closed system.

Petroff 2017). In the next few years, these FRB catalogues will grow by orders of magnitude with current and future surveys detecting thousands of events per year (Connor et al. 2016).

As radiation from an FRB propagates through the intervening gas, the free electrons in the gas retard the radiation. As the retardation of the radiation is frequency dependent, this process disperses the FRB pulse, thus producing a measurable time delay between the highest and lowest radio frequencies of the pulse. The dispersion measure quantifies this time delay. The dispersion measure, from observations of the photon arrival time as a function of frequency, is given by

$$\int (1+z)\, n_{\rm e}\, {\rm d}r, \tag{2}$$

which provides an integral constraint on the free electron density, $n_{\rm e}$, along the line of sight from the observer to the source, where dr is the path length in comoving coordinates. The free electron density and the radiation path in equation (2) are also in comoving units. The dispersion measure will include contributions from free electrons in the intergalactic medium (IGM) (Zheng et al. 2014; Shull & Danforth 2018), our galaxy, the Local Group, the galaxy hosting the FRB, and baryons residing in other galactic haloes which intersect the sightline (McQuinn 2014). As such, FRBs provide a possible way to investigate the presence of baryons that are difficult to observe with other methods.

In hydrodynamical simulations, we can calculate contributions to the dispersion measure from both the ISM and the hot halo of MW-like galaxies, and investigate the model dependence. The electron column density can be calculated for sightlines in a similar way to that described in Section 7.1 below. We calculate the number of free electrons for each gaseous particle or cell in the simulations by computing the number density of H II, He II, and He III, which dominate the total electron density; these calculations again utilize the ion fraction lookup tables of Hummels et al. (2017).

4 BARYON EVOLUTION

As we have shown in Section 2, APOSTLE and AURIGA produce galaxies in MW-mass haloes that have roughly similar morphologies, stellar masses, and stellar mass distributions. However, as the simulations are calibrated to reproduce a number of stellar properties of the observed galaxy population, these similarities are not too surprising. In this section, we explore the effects of the two different hydrodynamical schemes and feedback implementations on the *untuned* baryon properties. In particular, we investigate the baryon fraction around the two pairs of MW and M31 analogues and how this evolves with both radius and time.

In Fig. 4, we investigate the baryon fraction within a sphere centred on the main progenitors of the AP-S5-N1 simulations, as a function of radius at six different redshifts. Even though both simulations follow the assembly of the same dark matter halo, the baryon fraction within a sphere of radius ≈500 kpc (comoving) begins to differ significantly between $z = 8$ and $z = 5$. By $z = 2$ the APOSTLE model has developed a baryon deficiency of ≥ 10 per cent within a radius of ≥1 Mpc (comoving), extending to ≈2 Mpc at the present day. We refer to this is the Local Group baryon deficiency. By contrast, in the AURIGA simulations the baryon fraction is within 10 per cent of unity for radii ≥0.5 Mpc (comoving) at all redshifts. Furthermore, the minimum baryon fraction within a sphere around the primary AURIGA galaxy is ≈ 80 per cent, approximately twice that of its APOSTLE counterpart.

In Table 1, the baryon fraction of AP-V1-N1-Ea is similar ($\sim 0.85\Omega_{\rm b}/\Omega_{\rm m}$) to that of the AURIGA counterpart. However, the baryon fraction of this galaxy at $z = 1$ was $\sim 0.5\Omega_{\rm b}/\Omega_{\rm m}$, almost a factor of two lower than in AURIGA. Furthermore, the baryon fraction within a radius of ∼1 Mpc is ∼ 30 per cent lower than in AURIGA. Thus, even the most baryon-rich halo in APOSTLE is still baryon poor compared to the same halo in AURIGA. The differences in the baryon fraction of the haloes in the local region, out to ∼1 Mpc, around AP-S5-N1 are representative of the sample. Thus, while we focus on the individual halo AP-S5-N1 for illustration, the general results are valid for all haloes in our sample.

In both APOSTLE and AURIGA the halo baryon deficiency peaks at around $z = 1$–2, which is consistent with the observed peak in the star formation rate in the real universe (Madau & Dickinson 2014). However, the amplitude, spatial extent, and scale of the baryon deficiency in APOSTLE, compared to AURIGA, is striking. This difference is particularly remarkable given that the primary galaxies are relatively similar.

AGNs feedback is often thought to be the cause of low baryon fractions in MW-mass, and more massive haloes in cosmological hydrodynamical simulations (Bower et al. 2017; Nelson et al. 2018; Davies et al. 2019). Nevertheless, we see from Fig. 4 that the decrease

in baryon fraction in APOSTLE sets in at high redshift when the halo masses, and thus the black hole masses, are much lower. These results thus imply a different driver for the low baryon fractions at early times. While these haloes are already baryon deficient early in their evolution, the addition of AGNs feedback can further decrease the baryon fraction. As described, the AGNs feedback in APOSTLE is weaker than that found in EAGLE, which can explain why the APOSTLE haloes are almost twice as baryon rich as those in the EAGLE reference model.

Although the two simulations predict very different local baryon fractions, both within the halo and beyond, it is difficult to ascertain which of these models is the more *realistic*. In practice, it is very difficult to infer the baryon fractions of real galaxies. For external galaxies this are typically derived from X-ray emission using surface brightness maps to infer a gas density profile. These inferences also require information about the temperature and metallicity profiles, which are difficult to measure accurately with current instruments (Bregman et al. 2018).

In the MW, the baryonic mass in stars, cold and mildly photoionized gas and dust is estimated to be 0.65×10^{11} $M_\odot$ (McMillan 2011). The total mass of the halo, which is dominated by dark matter, is estimated to be $(1.17 \pm 0.15) \times 10^{12}$ $M_\odot$ (Callingham et al. 2019). Assuming a universal baryon fraction of $\Omega_b/\Omega_m \approx 0.157$ (Planck Collaboration XI 2013) implies that 0.8×10^{11} $M_\odot$ of the MW's baryons are unaccounted for. There is strong evidence that some fraction of these unaccounted baryons resides in a hot gaseous corona surrounding massive haloes; however, the total mass remains uncertain. An accurate estimate of the mass of the MW hot halo requires knowledge of the gas density profile as a function of radius. While the column density distribution of electrons is constrained in the direction towards the Large Magellanic Cloud (Anderson & Bregman 2010), there is a degeneracy between the normalization and the slope of the electron density profile (Bregman et al. 2018). Assuming a flat density profile (e.g. Gupta et al. 2012, 2014; Faerman, Sternberg & McKee 2017), the MW appears to be 'baryonically closed'. However, for faster declining density profiles (see Miller & Bregman 2015; Li & Bregman 2017), the gaseous halo out to R_{200} contains only half of the unaccounted baryons. Therefore, the predictions of Fig. 4 for both APOSTLE and AURIGA are consistent with observations given the uncertainties.

5 THE MISSING HALO BARYONS

In this section, we carry out a detailed analysis, on a particle-by-particle basis, of the differences in the present-day baryon contents of the APOSTLE and AURIGA Local Group analogues. As we described in Section 3.2, each dark matter particle is assigned a gas particle, or a tracer particle, which shares the same Lagrangian region in the ICs. In the absence of baryonic physics, these particles would evolve purely under gravity and would thus end up in the same halo as their dark matter counterparts. We refer to these as 'pre-destined' particles. However, hydrodynamics and feedback will significantly alter their fate.

We start our analysis by identifying all the dark matter particles present in each of the primary haloes at $z = 0$. We then identify the baryonic companions of these dark matter halo particles and categorize their $z = 0$ state, as illustrated in Fig. 5, classifying them into the following four categories:

(i) **Halo gas:** gas particles within R_{200} of the primary halo
(ii) **Halo stars:** star particles within R_{200} of the primary halo

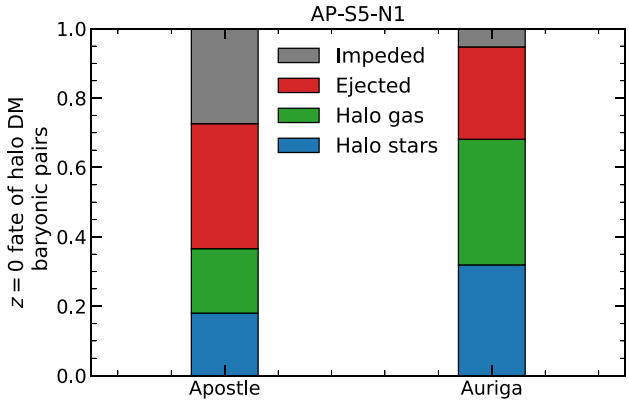

Figure 5. The present-day fate of the baryonic counterparts of the dark matter particles within R_{200} of the primary halo AP-S5-N1 in APOSTLE and AURIGA. The halo stars, halo gas, ejected gas, and impeded gas are shown by blue, green, red, and grey bars, respectively. See the text for a detailed description of these categories.

(iii) **Ejected gas:** gas particles which are outside R_{200} at $z = 0$ but had closest approach radii smaller than R_{200} at a previous redshift
(iv) **Impeded gas:** gas particles which are outside R_{200} at $z = 0$ and had closest approach radii larger than R_{200} at all previous redshifts.

It is important to note that Fig. 5 does not include baryons in the present-day halo if the dark matter counterpart is not in the halo. These baryons make a negligible contribution to the halo baryon mass.

There are several important differences in Fig. 5 between APOSTLE and AURIGA. About 35 per cent of the baryonic pairs of the $z = 0$ dark matter halo particles lie inside the primary halo of the APOSTLE simulation, whereas in the AURIGA simulations approximately 70 per cent of the baryon counterparts are within R_{200}. The baryons that lie within the halo are split between stars and gas in a roughly 1: 1 ratio in both simulations.

While the fate of the retained baryon counterparts is similar in the two simulations, the evolution of the absent baryons is considerably different. In APOSTLE we find that almost half of the baryon counterparts which are missing *never entered the halo*, whereas in AURIGA almost ≈ 90 per cent of the absent baryons entered the halo before being ejected, presumably by SNe or AGNs feedback.

5.1 Ejected gas

In Figs 6(a) and (b) we show the evolution of 10 randomly selected 'pre-destined' halo baryons which have been classified as 'ejected'. The particles are sampled at 60 snapshots linearly spaced as a function of the age of the universe, corresponding to a temporal resolution of $\approx$200 Myr.

In both simulations we see that the radial trajectories of both the gas and paired dark matter particles are generally very similar at early times. As the dark matter and baryon counterparts get closer to the main halo, their paths deviate and there is a tendency for gas accretion to be delayed relative to dark matter.

Following accretion into the halo, the trajectory of the gas begins to differ significantly from that of the dark matter. This deviation is caused by hydrodynamical forces which determine the subsequent evolution of the baryons. Most of the baryonic particles sampled in Figs 6(a) and (b) reach a high density upon accretion and increase

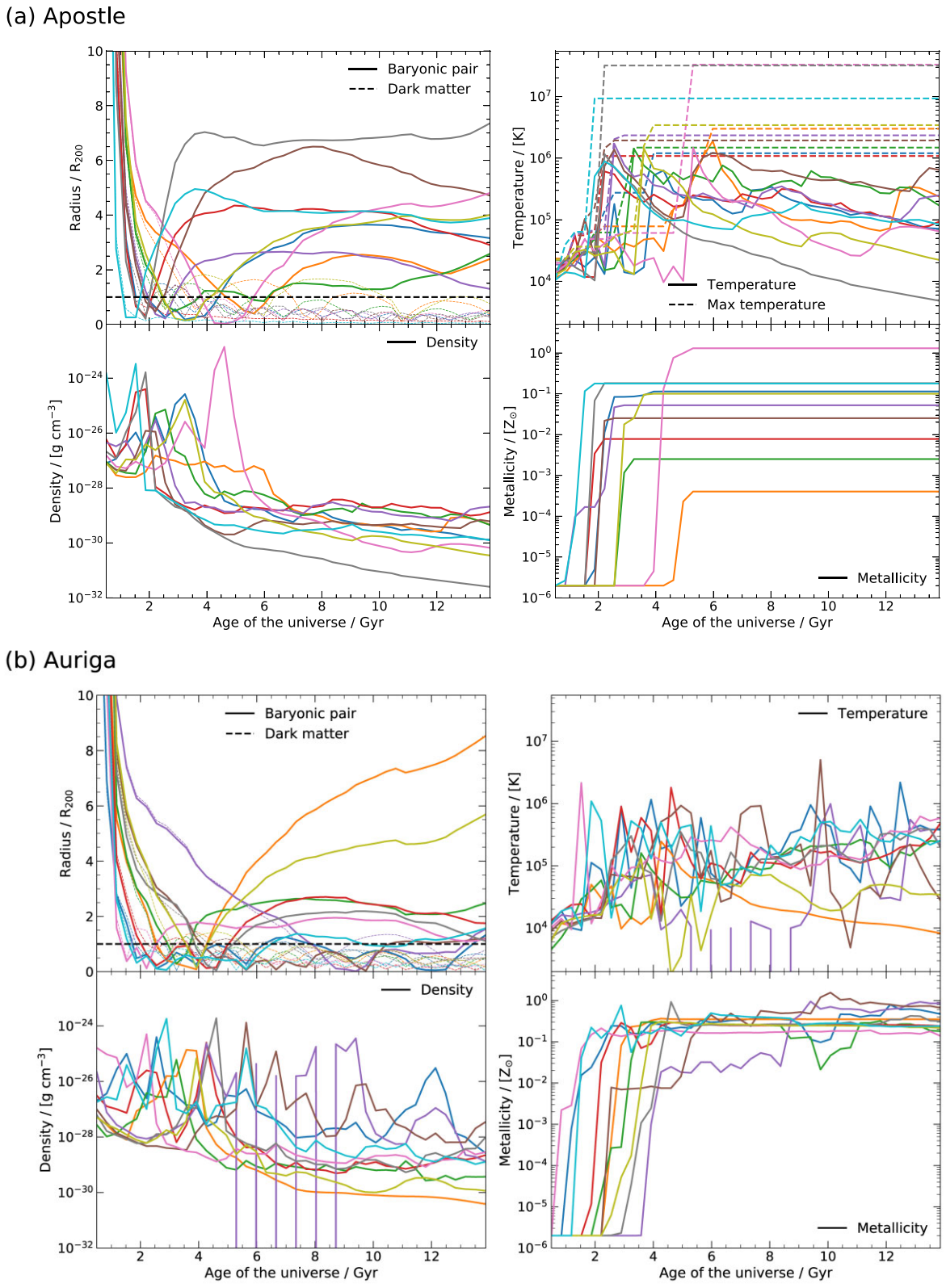

Figure 6. The evolution of 10 randomly selected halo baryonic tracer particles classified as 'ejected' from an (a) APOSTLE and (b) AURIGA halo. For both (a) and (b), the top-left, top-right, bottom-left, and bottom-right panels show the radius from halo centre, mean temperature, density, and metallicity as a function of time. The particle properties are sampled at 60 snapshots linearly spaced as a function of the age of the universe. The radius is given in units of $R_{200}(z)$. The top-left panel also includes the radial position of the dark matter counterpart of each baryon particle; these are illustrated with a dashed line of the same colour. In the bottom-right panel, which shows the metallicity, there are several lines which lay on top of one another and thus are not visible. The same random particle is identified in each panel by the same coloured line.

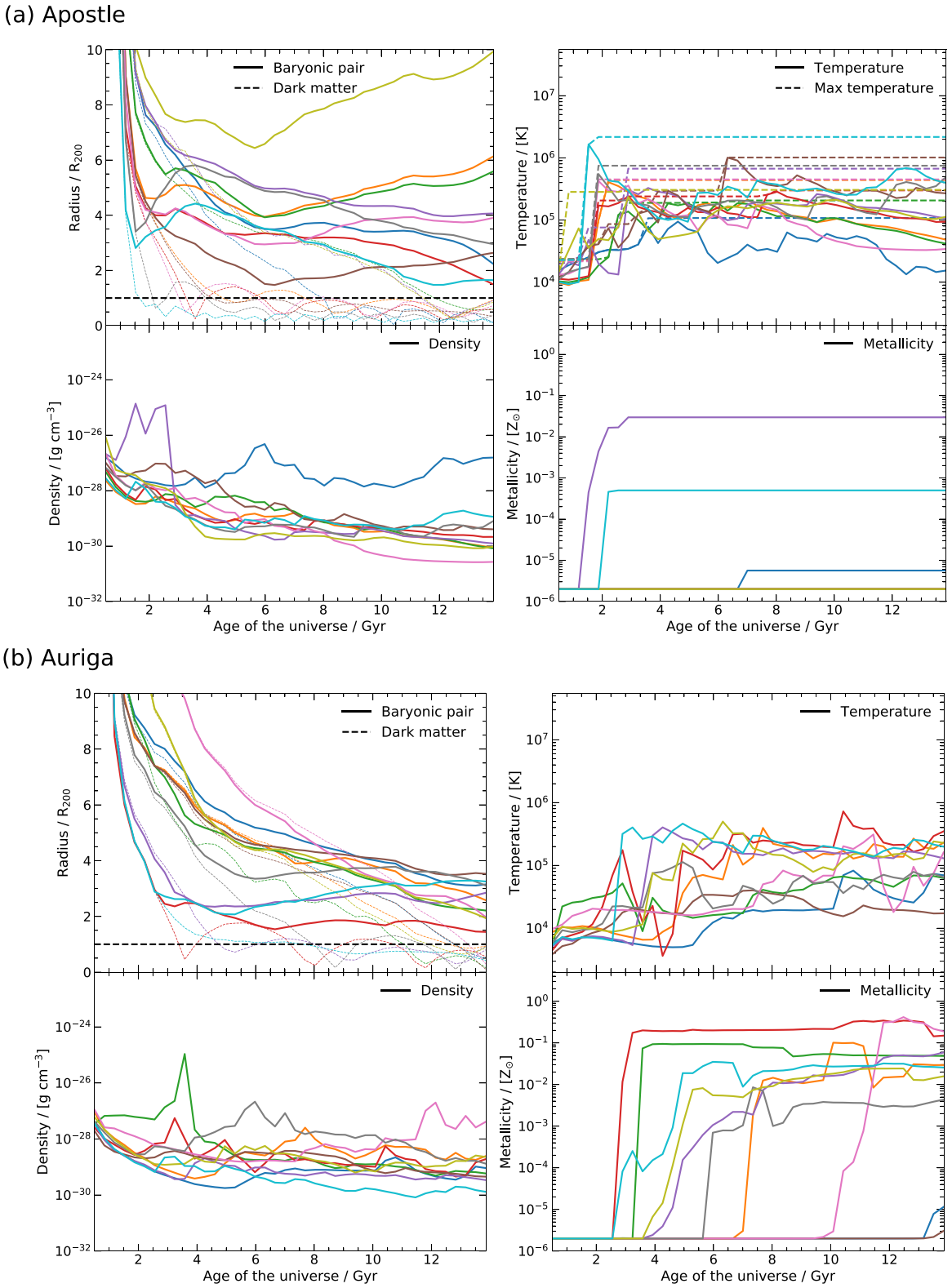

Figure 7. The evolution of 10 randomly selected halo baryonic tracer particles classified as 'impeded' from an (a) APOSTLE and (b) AURIGA halo. For both (a) and (b), the top-left, top-right, bottom-left, and bottom-right panels show the radius from halo centre, temperature, density, and metallicity as a function of time. The particle properties are sampled at 60 snapshots linearly spaced as a function of the age of the universe. The radius is normalized to the (time-dependent) R_{200}. The top-left panel also includes the radial position of the dark matter counterpart of each baryon particle; these are illustrated with a dashed line of the same colour. In the bottom-right panel, which shows the metallicity, there are several lines which lay on top of one another and thus are not visible. As with Fig. 6 the same random particle is identified in each panel by the same coloured line.

their metallicity. This behaviour is consistent with halo gas that has cooled, been accreted on to the central galaxy and later ejected.

Focusing first on APOSTLE, Fig. 6(a), we see that most of the randomly selected 'ejected' particles were ejected over 6 Gyr ago. In general, these particles reach a maximum radius, and near-constant, separation of $\approx$(3–8)R_{200} very quickly. At the present day, this corresponds to a physical distance of $\approx$(500–1500) kpc and is consistent with the conclusions of Section 4 which reveals a baryon-deficient Local Group on scales of up to 2 Mpc. There also appears to be a general trend in that the earlier the gas ejection, the greater its radial separation from the primary galaxy.

Fig. 6(a) shows that prior to being ejected, most of the APOSTLE gas was cold but then underwent a sudden temperature increase, with maximum temperatures regularly exceeding 10^7 K. The ejection of the gas from the halo rapidly follows the temperature increase. This process most likely proceeds as follows: the cold gas is part of the galaxy's ISM; some of it is heated to a temperature $T \geq 10^7$ K either directly by SNe feedback or indirectly by interaction with a SNe-heated particle. The hot gas then gains energy and is accelerated to a velocity that exceeds the escape velocity of the halo. This gas can then escape beyond R_{200} and join the low-density IGM where it remains until the present day. It is interesting that much of the ejected gas does not have a maximum temperature, $T = 10^{7.5}$ K. This indicates that this gas was not directly heated by SNe but rather by interactions with SNe-heated gas.

In Fig. 6(b), we see that the evolution of both baryons and dark matter is similar in AURIGA and APOSTLE before ejection. However, in AURIGA, the ejected gas typically reaches a maximum radial distance of $\sim 3R_{200}$ before turning back and falling into the halo by the present day. Thus, the 'ejected' gas in AURIGA likely has a shorter recycling time-scale than the gas in APOSTLE, much of which never re-enters the halo. However, gas that was ejected at early times and re-accreted is not, by definition, included in Fig. 6(b). Short recycling times in AURIGA were first reported by Grand et al. (2019) who show the model gives rise to efficient galactic fountains within the inner $\sim$30 kpc, with median recycling times of $\sim$500 Myr in MW-mass haloes.

5.2 Impeded gas

We now analyse the evolution of 10 randomly selected 'pre-destined', baryonic particles which have *never* entered the primary halo. These are plotted in Figs 7(a) and (b) for APOSTLE and AURIGA, respectively. In Fig. 7(a), we see that about half the randomly selected particles in APOSTLE make their initial approach at redshift, $z \sim 2$–3. As the dark matter particles are accreted into the halo, their baryon counterparts start being impeded at a radius $\sim 4R_{200}$. The subsequent fate of these particles can differ substantially. About half of them remain at a distance $\geq 3R_{200}$ until the present day, whereas the other half continue to approach the primary halo and are almost accreted by $z = 0$.

The (maximum) temperature of the 'pre-destined' impeded particles in APOSTLE is shown in the top-right panel of Fig. 7(a). The overall temperature evolution of all impeded particles is quantitatively similar. Initially, the gas is at low temperature, $\approx 10^4$ K, but as it approaches the halo, it is subject to an almost instantaneous temperature rise to $\approx 10^6$ K. Since the maximum temperature of the gas is always well below $10^{7.5}$ K, this rise is not the result of direct SNe or AGNs heating. Furthermore, before closest approach, these gas particles also have low density and metallicity, with one or two exceptions. These properties are consistent with pristine gas within the IGM, thus confirming that direct feedback did not heat these particles.

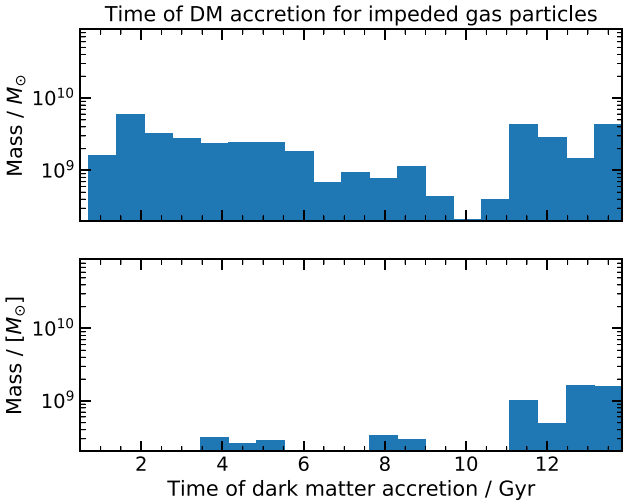

Figure 8. Mass-weighted histogram of the age of the universe at the time of accretion of the dark matter particles associated with 'pre-destined' baryon particles that have been *impeded*. The top panel shows results for the AP-S5-N1 halo in APOSTLE and the bottom panel for AURIGA. This shows that cosmic gas accretion is significantly impeded at all times in APOSTLE, whereas AURIGA only impedes cosmic gas accretion, relative to dark matter accretion, at late times.

In Fig. 7(b), we see that the accretion time of the dark matter counterparts of the 10 randomly selected impeded baryons in AURIGA is recent, within the last $\approx$4 Gyr, for most particles. In APOSTLE we saw that before closest approach, the baryon particles were relatively unenriched, cold and at low density showing no sign of interaction with nearby galaxies. However, as seen in the bottom-right panel of Fig. 7(b), much of the impeded gas in AURIGA is enriched; this suggests the cause of the impediment could be interactions with other nearby galaxies at earlier times. The impeded gas could have been accreted by these galaxies or have interacted with their winds.

In Fig. 8, we show the mass-weighted distribution of first accretion times of all dark matter particles associated with 'pre-destined' baryon particles classified as 'impeded'. The APOSTLE simulations have a weakly bimodal distribution: the dark matter associated with impeded gas was accreted either at early or at late times. In the AURIGA simulations the late accreted population dominates.

The presence of hot quasi-hydrostatic haloes can impede gas accretion at late times. Haloes of mass $\gtrapprox 10^{12}$ $M_\odot$ have massive hot gaseous coronae. These gaseous haloes, which often extend beyond R_{200}, can exert pressure on the accreting gas and thus delay its accretion. The accretion of the collisionless dark matter is, of course, not impeded. The process impeding gas accretion at early times and late time in APOSTLE is likely to be similar. However, the progenitors of the present-day primary haloes are not massive enough at high redshift to support massive atmospheres of primordial gas to explain the observed scale of suppressed accretion so most of the gaseous atmosphere must be gas that was reheated and ejected.

The explanation is provided in Fig. 9 which shows temperature projections of the AP-S5-N1 halo at four times between $z = 3.5$ and $z = 2$ in both APOSTLE and AURIGA. We overlay the positions of 16 randomly selected baryon/dark matter pairs chosen so that they were 'impeded' at early times in APOSTLE. The same pairs, originating from the same Lagrangian region in AURIGA, are also overlaid. The blue circles show the x, y positions of the dark matter and the white circles those of the baryons. The white dotted line

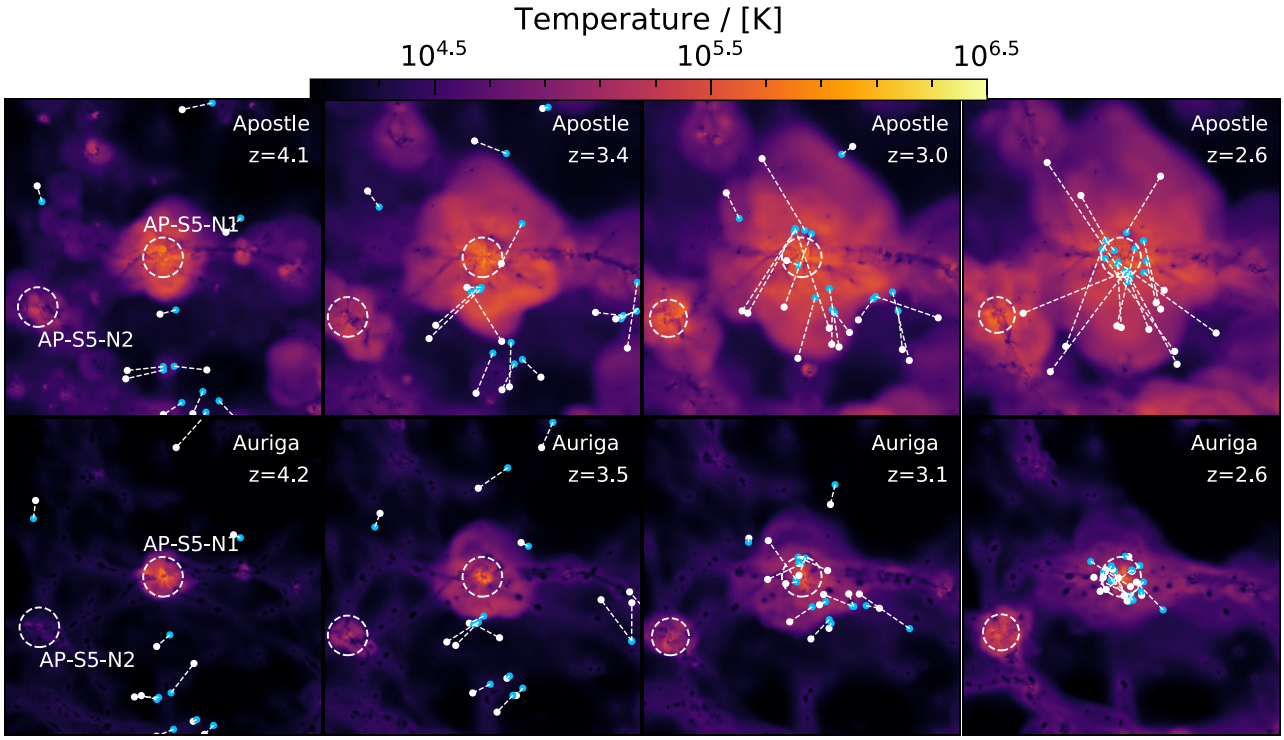

Figure 9. Mass-weighted temperature projections through a region of size (16 × 16 × 24) R_{200} centred on the location of the progenitor of the primary galaxy in AP-S5-N1 at four redshifts, $z \sim 4$, 3.5, 3, 2.5. Results are shown for both APOSTLE (top row) and AURIGA (bottom row). The white and blue circles show the positions of 16 randomly selected baryon-dark matter counterparts which are 'impeded' at early times in APOSTLE. The same counterparts, originating from the same Lagrangian region, are shown in AURIGA. The white dotted lines connect the baryon/dark matter counterparts. The white dashed circles identifies the R_{200} of the two main haloes.

connects the baryon/dark matter pairs to help visualize the differences in the evolution of the two species.

We see that in APOSTLE the MW progenitors are encased in a hot, $\approx 10^6$ K, corona of gas that occupies a volume of radius twice as large as that of the AURIGA counterparts. This gas halo consists of a mixture of accreting primordial gas and hot outflowing winds fuelled by feedback from the central galaxy. As shown in Fig. 6, gas particles in the ISM can be heated by SNe feedback, generating a hot, outflowing wind that can reach distances of up to $4R_{200}$ in less than 1 Gyr. This outflowing gas interacts with the accreting gas, applying an outward force sufficient to delay or prevent accretion. This leads to large amounts of 'pre-destined' gas 'impeded' from accreting at early times in APOSTLE (as seen in Fig. 5). The overlaid particles in Fig. 9 succinctly demonstrate this process.

In contrast, the AURIGA haloes have hot gaseous components that barely extend beyond R_{200} and do not evolve in time significantly. As the hot component in AURIGA is less massive and cooler than in APOSTLE, the dark matter/baryon pairs evolve similarly until they reach $\sim 1.5R_{200}$. At radii $\leq 1.5R_{200}$ gas accretion is delayed relative to the dark matter by hydrodynamical forces. However, it appears less than 5 per cent of gas is completely prevented from accretion.

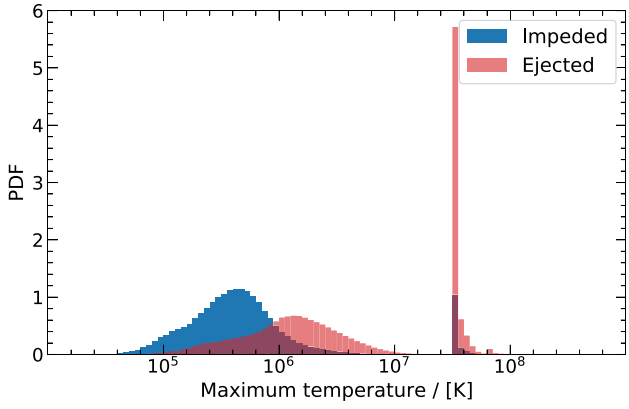

Figure 10. A normalized histogram of the logarithmic maximum historical temperature of all the ejected (red) and impeded (blue) gas particles identified in the AP-S5-N1 halo of the APOSTLE simulation. The maximum temperature is the highest temperature recorded throughout the entire simulation. We do not show the maximum temperature for the tracer particles in AURIGA as the tracer particles do not store this information.

5.3 Quantitative sample properties

This section quantifies various statistics of the entire ejected and impeded gas components in the APOSTLE and AURIGA simulations of AP-S5-N1. While we only show results (Figs 10–13) for AP-S5-N1, these are representative of our sample of four MW-mass haloes.

It is worth reminding the reader that the ejected and impeded gas components are much smaller in AURIGA than APOSTLE.

In Fig. 10, we show the maximum temperature ever achieved by both ejected and impeded gas particles in the APOSTLE simulations. We find that only 35 per cent of the ejected gas particles have had a maximum temperature above $10^{7.5}$ K indicating direct heating by SNe or AGNs feedback. This demonstrates that most of the ejected

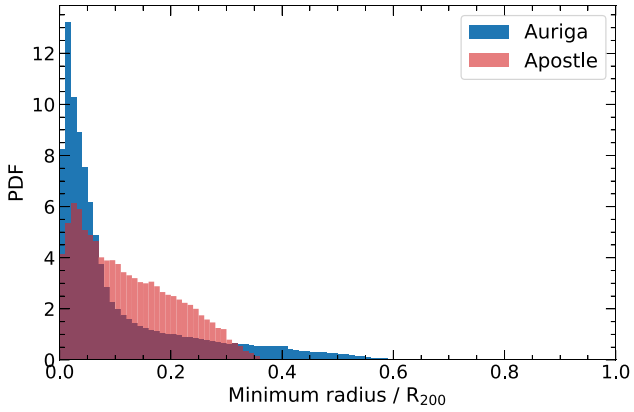

Figure 11. A normalized histogram of the minimum recorded galactocentric radius of all the ejected gas particles, prior to ejection, identified in the AP-S5-N1 volume of both APOSTLE (red) and AURIGA (blue).

gas was not directly heated but rather entrained by a wind. We also note that 0.03 per cent of the ejected gas was heated to temperatures of $10^{8.5}$ K. At face value this suggests that AGNs play a minor role in ejecting gas from the galaxies although we cannot exclude the possibility that a significant number of gas particles were indirectly heated by a few particles whose temperature was raised to a very high value by the AGNs, but were not ejected. The median maximum temperature of the impeded gas is roughly $10^{5.6}$ K which is consistent with the findings of Fig. 7 in which we suggest most of the impeded gas in APOSTLE is cold before being heated almost instantaneously to approximately 10^6 K as it approaches the halo. Unfortunately, this analysis cannot be repeated for the AURIGA simulations as the simulations do not track the maximum temperature.

In Fig. 11, we show the minimum radius of ejected gas particles in both APOSTLE and AURIGA prior to ejection. In AURIGA, we find that over 85 per cent of the ejected gas particles resided at a minimum radius $\leq 0.15R_{200}$, suggesting that these particles were ejected from the ISM of the galaxy. In APOSTLE we find 65 per cent of the ejected gas particles came from within $\leq 0.15R_{200}$. This again suggests that most of the ejected gas in APOSTLE comes from the ISM. Combining this with the result that SNe directly heated 35 per cent of the ejected gas suggests that about half of the entrained gas in APOSTLE comes from the ISM, and the rest from the CGM.

Fig. 12 shows the radius of both ejected and impeded gas particles, at the present day, in both APOSTLE and AURIGA. We see that almost 70 per cent of the ejected gas in AURIGA resides within a radius $\leq 2R_{200}$ at the present day. In contrast, only 30 per cent of the APOSTLE ejected gas resides within this radius. This is in agreement with the results of the randomly selected particles in Fig. 6 and demonstrates the significant difference in the fate of the ejected gas between the two simulations. The results of the impeded gas are similar. In AURIGA, which has much less impeded gas, we see that 75 per cent of the impeded gas is within $3R_{200}$, and a considerable portion of this has been accreted by a nearby galaxy. Again, APOSTLE shows a much more extended distribution of impeded gas with only 35 per cent of the impeded gas within $3R_{200}$ at the present day. This supports the results of Fig. 7 for a small random sample of particles.

Finally, we look at the present-day metallicity of all the ejected and impeded gas particles, in both APOSTLE and AURIGA, in Fig. 13. We first describe the metallicity of the ejected gas. In AURIGA around 80 per cent of the ejected particles have a metallicity ≥ 0.1 $Z_\odot$. In APOSTLE, about 60 per cent of the ejected particles have a metallicity ≥ 0.1 $Z_\odot$. Both of these results are consistent with the fraction of ejected particles with a minimum radius $\leq 0.15R_{200}$. These results suggest that the mass loading factor in APOSTLE is likely higher than in AURIGA. The impeded gas in APOSTLE is almost entirely pristine with over 70 per cent of the gas having metallicity $\leq 10^{-5}$ $Z_\odot$. Conversely, 30 per cent of the impeded gas in AURIGA has metallicity above ≥ 0.1 $Z_\odot$. It appears that much of the impeded gas in AURIGA has directly interacted with a nearby galaxy, or the wind of a nearby galaxy, causing metal enrichment. The results of Fig. 7 suggest that a significant fraction of the impeded gas in AURIGA may have been stripped from progenitors of the main halo, explaining their enrichment.

5.4 The fate of impeded and ejected baryons

Fig. 14 shows the projected dark matter and gas density of both 'ejected' and 'impeded' baryons that were 'pre-destined' to end up in the primary halo but are missing. In the APOSTLE simulations, the present-day distribution of these missing baryons is different for the 'impeded' and 'ejected' components. The impeded gas appears to be elongated roughly along the x-axis which, as can be seen in the projected dark matter distribution, traces a local filament. By contrast, the ejected gas tends to be elongated along the y-axis, that is, perpendicular to the filament.

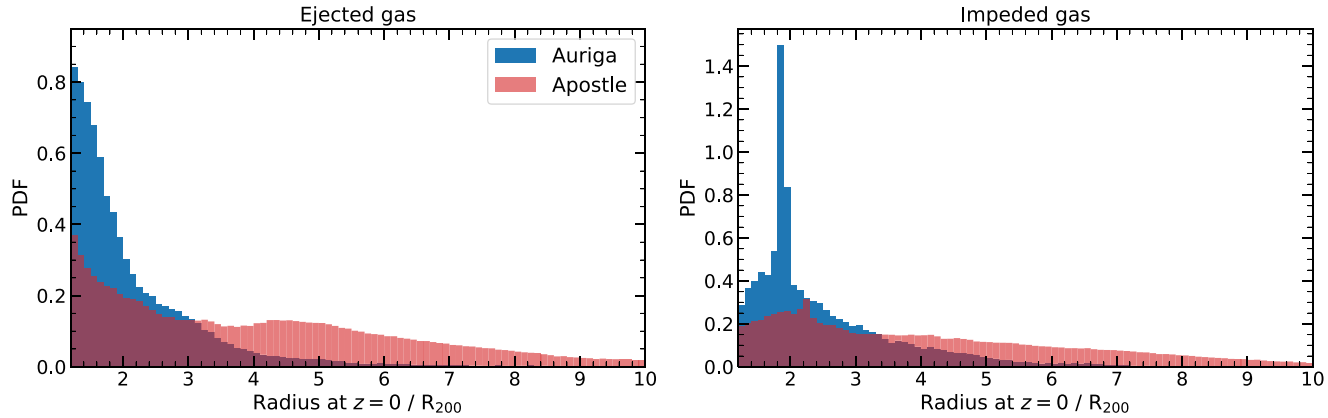

Figure 12. A normalized histogram of the present-day galactocentric radius of all the ejected (left) and impeded (right) gas particles identified in the AP-S5-N1 volume of both APOSTLE (red) and AURIGA (blue).

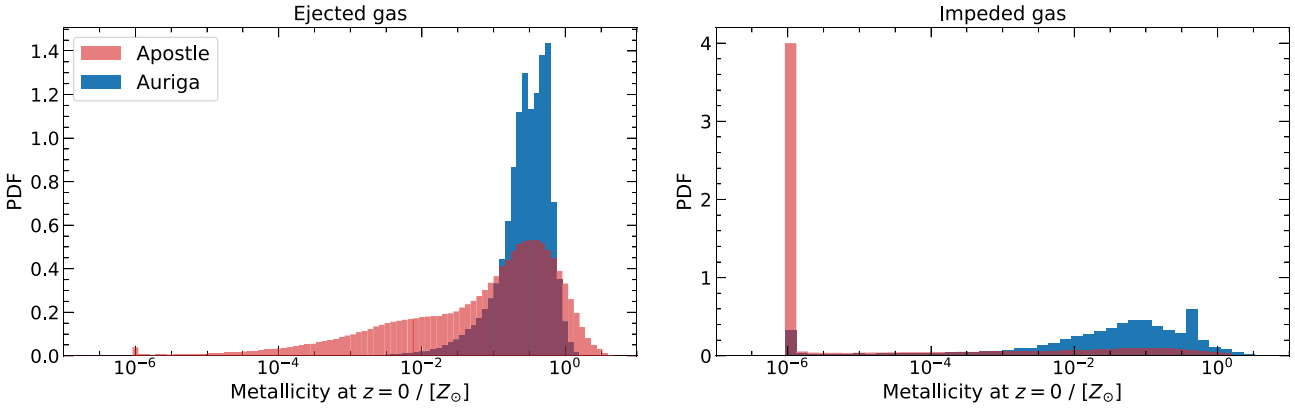

Figure 13. A normalized histogram of the present-day, $z = 0$, logarithmic metallicity of all the ejected (left) and impeded (right) gas particles identified in the AP-S5-N1 volume of both APOSTLE (red) and AURIGA (blue). We set the minimum metallicity to be 10^{-6} $Z_\odot$ to ensure inclusion in the histogram.

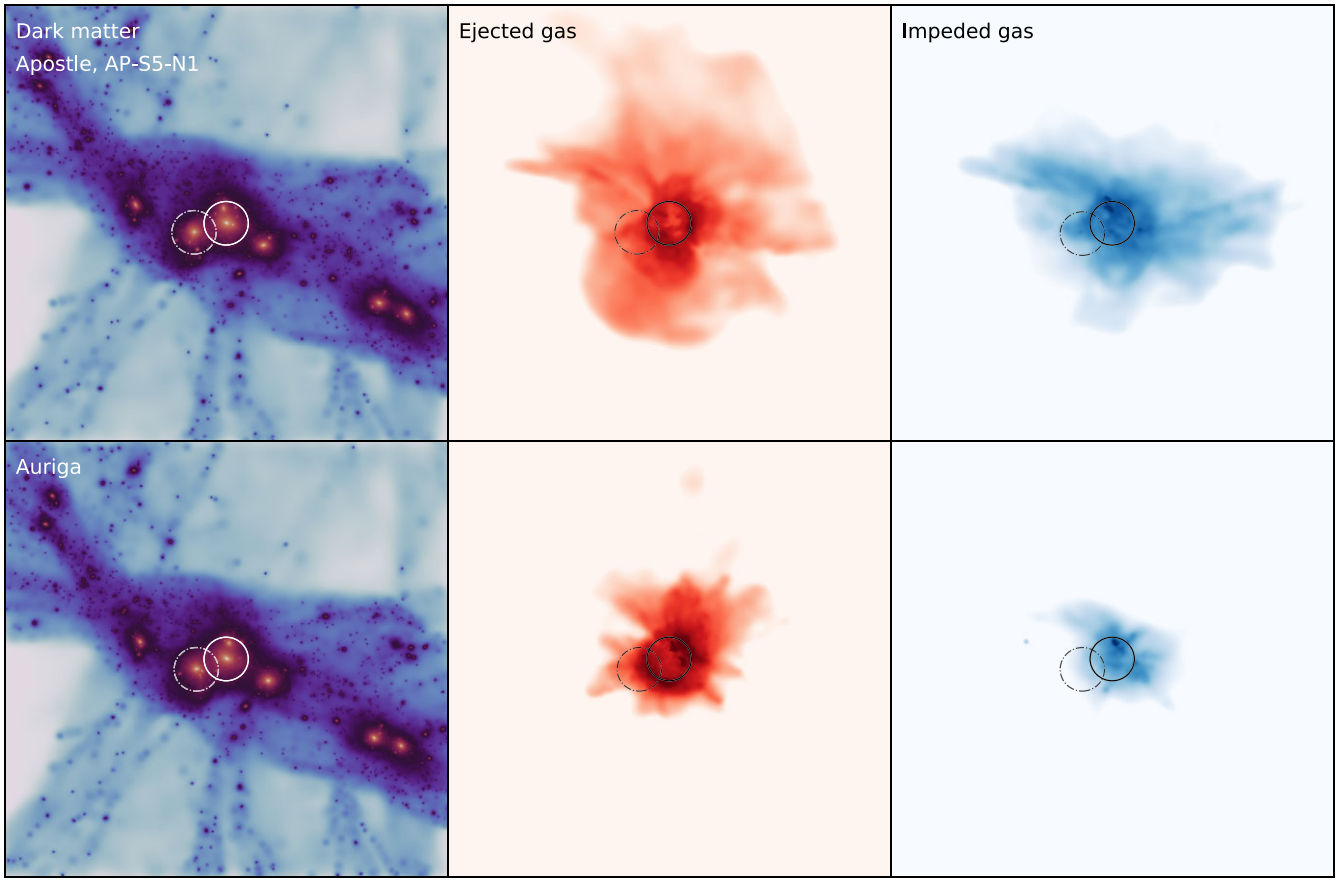

Figure 14. The $z = 0$ projected density of dark matter (left), ejected baryons (centre), and impeded baryons (right) for the AP-S5-N1 halo in both APOSTLE (top) and AURIGA (bottom). The projected cuboid has dimensions of $20 \times 20 \times 8$ R_{200} in the x, y, and z directions, respectively. The solid white/black circles indicate R_{200} of the halo AP-S5-N1 and the dash–dotted circles that of AP-S5-N2.

The reason for this apparent difference in the different distributions of impeded and ejected gas may be because the impeded gas flows towards the halo along the filament and would have been accreted by the halo had the pressure of the hot halo not impeded it. Thus, it remains in the filament, centred around the halo. The ejected material, on the other hand, finds the path of least resistance, which is perpendicular to the filament: along the filament direction the wind encounters relatively high-density gas, while in the perpendicular direction, the density and pressure of the surrounding medium drop rapidly. As a result, gas ejected perpendicular to the filament can reach larger radii, giving rise to the apparent elongated distribution seen in Fig. 14. However, Fig. 14 is not sufficient to prove this process happens; analysis of the surface density profiles along and perpendicular to the filament could quantitatively demonstrate this effect.

An interesting detail in Fig. 14 is the transfer of baryons between the M31 and MW analogues. This is due primarily to the effect of gas ejection from both galaxies which can cause cross-contamination. This process is an example of halo gas transfer (see Borrow et al. 2020) and indicates that the proximity of M31 may have influenced the evolution of the MW, although the amounts of gas transferred are very small.

While the two simulations predict very different morphologies for the ejected baryons, these differences are likely undetectable in the real universe because of the low density of ejected material.

6 UNDERSTANDING THE DIFFERENCES

In Fig. 15, we show histograms of the gas density and temperature weighted by mass, metal mass, and radial velocity for both APOSTLE and AURIGA at four redshifts. All gas particles/cells within a sphere of radius 3 R_{200} around the centre of the primary halo of AP-S5-N1 are included. As in Section 4, we focus on this particular example but our general results are valid for all haloes in our sample.

We can see in the figure the gas responsible for impeding accretion in APOSTLE at $z = 2$–3: it is hot, $\geq 10^6$ K, low density, $\sim 10^{-4}$ cm^{-3}, slightly metal-enriched, and outflowing with a mean radial velocity exceeding 100 km s^{-1} relative to the centre of mass of the halo. This gas component is visible from $z = 3$ until $z = 1$. In AURIGA gas with similar temperature and density is less enriched and is not outflowing. There is some hot enriched gas with large outflow velocities at all redshift, but this gas appears to cool and mix with inflowing material as there is no evidence of less dense and slightly cooler outflows.

At higher redshift, the majority of the metals in Fig. 15(b) reside in hot, diffuse gas. As shown by Fig. 15(c) this material is outflowing. Interestingly, we do not see any evidence of a significant cooler metal component developing until about $z = 1$–2. When this cooler metal component appears, it is radially inflowing, suggesting the recycling of earlier outflows.

In AURIGA we first see a population of metal-enriched gas that is both hot and dense at approximately $z = 3$. By $z = 2$, this enriched gas appears to have cooled and increased in density. This is inferred from distribution of metals. These features suggest the presence of galactic fountains even at high redshift. The AURIGA haloes also contain a component of very dense gas, $n_{\rm H} \geq 10^{-2}$ cm^{-3}, with temperature in the range $T \approx 10^4$–10^7 K. This is a further indication of efficient galactic fountains: the high densities lead to short cooling times, of order $\sim$200 Myr, and, for this substantial amount of gas to be present, it must be continuously replenished by the heating of dense gas by feedback.

The differences in the nature of outflows in APOSTLE and AURIGA could be due to differences in the SNe subgrid models. The APOSTLE SNe feedback model specifies the temperature increase of gas particles. In this model, SNe energy is effectively saved up and released in concentrated form stochastically. This technique means that gas is heated to higher temperatures less frequently, thus preventing the overcooling problem (Dalla Vecchia & Schaye 2012); in AURIGA, the energy injected per unit mass of SNII is fixed. This difference in the model causes gas in APOSTLE to reach higher temperatures post-SNe feedback.

The total cooling efficiency of moderately enriched gas has a local minimum around a temperature of 10^7 K and increases quite steeply both with increasing and decreasing temperature (see e.g. fig. 9 of Baugh 2006). Thus, a post-feedback temperature lower than 10^7 K leads to both a higher cooling rate and lower thermal energy. When these effects are combined, the cooling time can be reduced by an order of magnitude or more. The lower post-feedback temperature in AURIGA could allow SNe-heated gas to radiate a significant fraction of the injected energy on a time-scale of order several hundred million years. This reduced cooling time would facilitate short recycling times for gas in AURIGA and prevent the build-up of a hot, SNe-fuelled atmosphere at high redshift.

In APOSTLE, by contrast, feedback heats the gas to $10^{7.5}$ K, and thus radiative cooling is relatively inefficient. Fig. 8 of Kelly et al. (2021) shows the density and temperature of gas particles 500 Myr before and after SNe heating in the EAGLE reference simulation. That figure shows that gas particles that experience SNe feedback decrease their density by over two orders of magnitude within $\leq$20 Myr of being heated. This expansion prevents efficient radiative cooling and also makes the gas buoyant so that it is accelerated out through the halo (Bower et al. 2017).

Fig. 16 shows a mass-weighted projection of the radial velocity of the gas in AP-S5-N1 for both APOSTLE (top row) and AURIGA (bottom row) at five redshifts, $z \sim 0, 1, 2, 3, 4$. It is clear from these projections that rapid outflowing material extends well beyond the halo, reaching distances of $\sim 4R_{200}$ at $z = 4$ in APOSTLE. These strong, halo-wide outflows are readily visible until $z = 1$. By contrast, in AURIGA the mass-weighted radial velocity of the outflows is much slower, and their spatial extent is smaller. These radial velocity projections indicate that APOSTLE haloes experience strong outflows with high covering fractions. A high outflow velocity, combined with a large covering fraction, can impede cosmological gas accretion on the scale of the entire halo. By contrast, in AURIGA we see less extended outflows because a significant fraction of the SNe-heated material cools and is efficiently recycled near the centre of the halo. van de Voort et al. (2021) show that the magnetic fields, included in the AURIGA simulations, can reduce the outflow velocities of gas around the central galaxies. This extra pressure from magnetic fields in AURIGA could be contributing to the reduced gas ejection from the halo compared to that found in APOSTLE.

Another factor that can vary the velocity and spatial extent of outflows is the potential depth. In Fig. 17, we show the approximate circular velocity profiles as a function of radius in the four primary haloes in both APOSTLE and AURIGA at $z = 0$. These approximate circular velocity profiles are calculated from the total enclosed mass assuming spherical symmetry. We see that in the inner 50 kpc the circular velocity is systematically higher in AURIGA, by up to as much as $\sim$100 km s^{-1}. This difference is because the APOSTLE model is much more efficient at driving winds from the central galaxy, propagating out to scales exceeding the virial radius (Mitchell et al. 2020a). This process reduces the density in the inner region, thus reducing the escape velocity and making future gas ejection more efficient. In AURIGA the opposite happens, as wind is inefficient at removing gas from the central region, the central density increases, thus deepening the potential well.

As described in Section 2, the gas dynamics in AURIGA are followed with a moving-mesh technique. Several studies have investigated the differences between moving-mesh and particle-based hydrodynamics techniques in the context of galaxy formation simulations (Kereš et al. 2012; Sijacki et al. 2012; Torrey et al. 2012; Vogelsberger et al. 2012; Bird et al. 2013; Nelson et al. 2013). A general result from these studies is that gas in moving-mesh simulations cools more efficiently than in their particle-based counterparts. The cooling efficiency of hot gas is artificially suppressed in particle-based simulations by spurious viscous heating and the viscous damping of SPH noise on small scales. Furthermore, moving-mesh

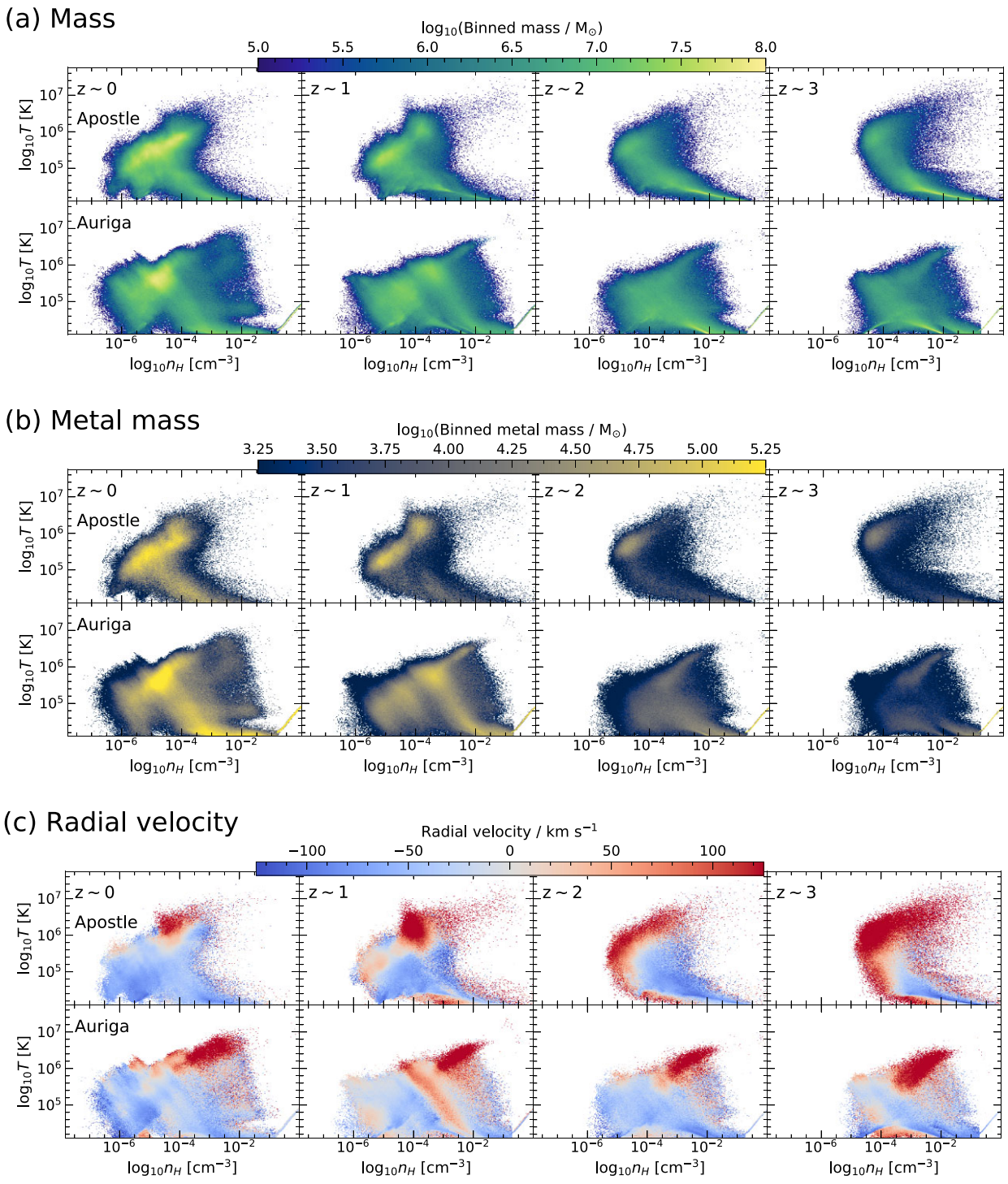

Figure 15. Gas density-temperature diagrams for a primary halo, AP-S5-N1, in both APOSTLE (top row) and AURIGA (bottom row). The histograms are coloured according to (a) mass, (b) metal mass, and (c) mass-weighted radial velocity. They include all gas with temperature $T > 10^4$ K that is within radius, $r < 3R_{200}$, of the primary halo. The four columns show the gas distributions at four redshifts, $z \sim 0$, 1, 2, 3, from left to right, respectively. The histograms are generated with 300 logarithmically spaced bins in the density range, 10^{-8}–1 cm^{-3}, and temperature range, $10^{3.5}$–$10^{7.5}$ K.

simulations model energy dissipation more realistically by allowing cascading to smaller spatial scales and higher densities (Nelson et al. 2013). As we mentioned earlier, we expect these difference to be subdominant to the large differences in the subgrid models between APOSTLE and AURIGA.

7 OBSERVATIONAL TESTS

We have shown in Sections 4 and 5 that the APOSTLE and AURIGA simulations predict very different baryon cycles around our MW and M31 analogues. We now turn to the observable signatures of strong outflows in APOSTLE and galactic fountains in AURIGA.

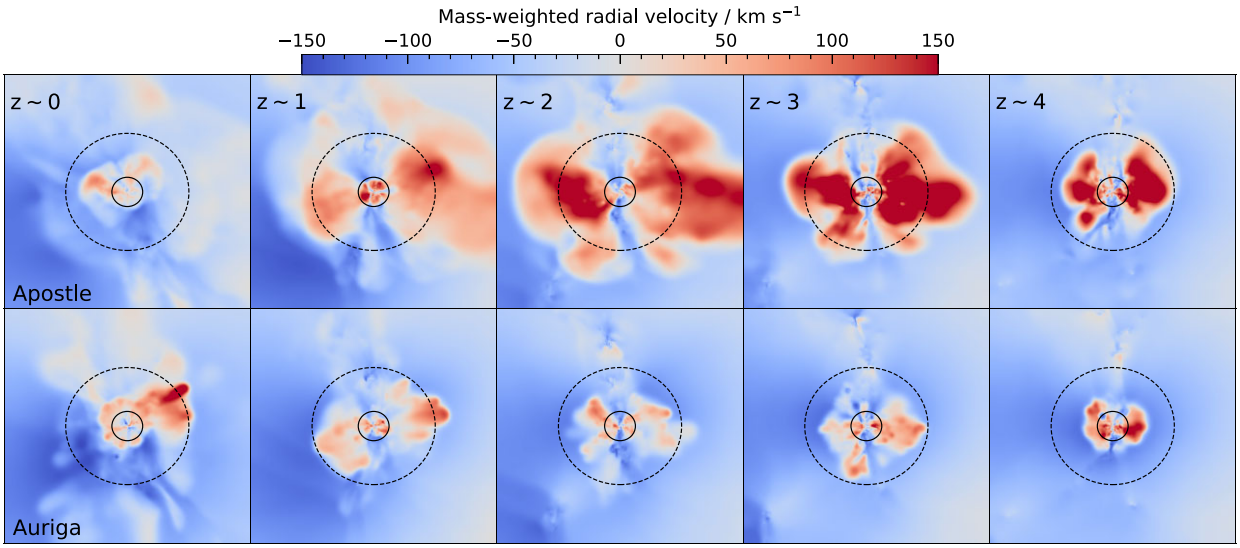

Figure 16. Mass-weighted projection of the radial gas velocity for AP-S5-N1 in both APOSTLE (top row) and AURIGA (bottom row) at five redshifts, $z \sim 0$, 1, 2, 3, 4, from left to right, respectively. The region of these projections has size $(16 \times 16 \times 2)$ R_{200} in the x, y, and z directions, respectively, where the z-axis is into the page. The solid black circle indicates R_{200} and the dashed back curve $4 \times R_{200}$.

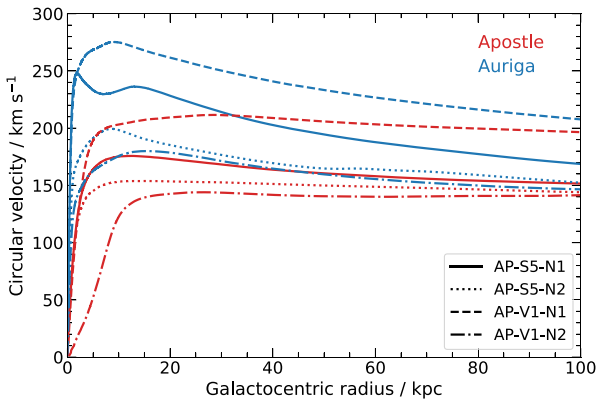

Figure 17. The approximate circular velocity of the four primary haloes in both APOSTLE and AURIGA at $z = 0$. The circular velocity, $V_{\rm circ}$, at radius r is calculated from the total enclosed mass, $M(< r)$, assuming spherical symmetry $V_{\rm circ}^2 = GM(< r)/r$, where G is the gravitational constant. The APOSTLE and AURIGA simulations are shown in red and blue, respectively.

We present mock observations of absorber column densities and dispersion measure around our MW and M31 analogues. We aim to construct mappings between the physical state of the baryons and real observables and, in particular, to identify observables that may be sensitive to the differences in the gas properties seen in the APOSTLE and AURIGA simulations.

7.1 Column densities

We show, in Fig. 18, the regions of the density–temperature plane where different species are relatively abundant. The contours enclose regions where each species contributes 10 per cent of the maximum ion fraction of the respective element in CIE at $z = 1$. We show these contours as they highlight regions of the density–temperature phase space where each species is likely to be detected. This analysis is similar to Wijers, Schaye & Oppenheimer (2020) which analysed lower resolution, large-volume cosmological simulations using the EAGLE galaxy formation model.

The species that probe the hottest gas, at $T \geq 10^6$ K, are typically O VII O VIII, and Mg X. However, there is a degeneracy as these ionization states are also plentiful in lower temperature, lower density gas. In the absence of other observables, it is difficult to distinguish whether detection of these ions is from a low-density or a high-density region. However, given that, in practice, the detection of these lines requires a moderately high column density, it is likely that any detection will be from gas at high density and, thus, high temperature. We also see in the figure that Ne VI, Ne VIII, and O VI probe a cooler component, at $T \leq 10^6$ K. This transition temperature, $T = 10^6$ K, is a significant threshold as it has the potential to distinguish hydrostatic gas at the virial temperature of MW-mass haloes from hotter gas heated by feedback energy.

The species O VII and O VIII are well suited for identifying very hot outflows. Unfortunately, these ions are challenging to observe in the real universe because the wavelengths of their lines are so short, ∼20 Å. These highly ionized stages of oxygen, the most abundant metal, have transitions that are detectable in X-rays. However, even modern X-ray instruments do not have the required resolution or sensitivity. Ne VI, Ne VIII Mg X, and O VI probe a similar, but typically cooler, component of gas, but have much longer transition wavelengths, e.g. 558, 770, 610, and 1032 Å, respectively. These are readily detectable with UV instruments and represent good probes of hot, collisionally ionized gas, easier to detect than than their X-ray counterparts, O VII and O VIII.

We now consider each of the ions considered in Fig. 19, one at a time. We begin with the column density profile of H I shown in the top row of Fig. 19. In general, the H I column density profile is similar at all redshifts in both simulations. The profile is centrally peaked and falls off rapidly, typically decreasing by about four orders of magnitude within the first 100 kpc, where it flattens to a near constant number density of 10^{15} cm^{-2}.

Between $z = 3$ and $z = 1$, the mean and scatter of the H I column density at fixed impact parameter agree well in both APOSTLE and AURIGA. However, at $z = 0$, there is a slight systematic offset in APOSTLE where the H I column densities are about a factor of five higher than in AURIGA. The offset diminishes in both the centre, <30 kpc, and beyond R_{200}. The similarity of the H I distributions in

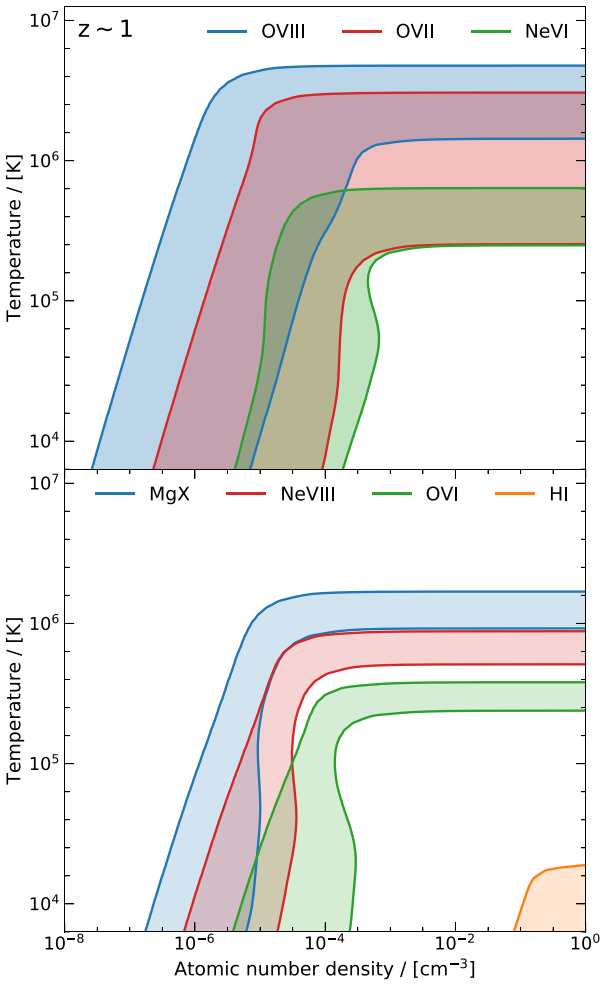

Figure 18. Temperatures and densities at which different metal species occur at $z = 1$. The ion fractions are calculated from the lookup tables of Hummels et al. (2017), assuming only radiation from the metagalactic UV background according to the model of Haardt & Madau (2012). These lookup tables are computed under the assumption of CIE. The contours for each of the indicated species are at 10 per cent of the maximum ion fraction. The top panel shows Ne VI (green), O VII (red), and O VIII (blue) and the bottom panel H I (orange), O VI (green), Ne VIII (red), and Mg X (blue).

both simulations is not surprising. In particular, we see in Fig. 15 that the distribution of gas at high densities and low temperatures, where H I typically occurs, is very similar in the two (see Fig. 18).

The second, third, and fourth rows from the top of Fig. 19 show the column density profiles of O VI, Ne VI, and Ne VIII, respectively. We discuss the distributions of these ions collectively, as they have similar general trends and typically probe gas at the same density and temperature, as demonstrated in Fig. 18. O VI, Ne VI, and Ne VIII probe progressively hotter populations of dense gas, increasing from $10^{5.5}$ up to 10^6 K. Ne VI typically probes a broader range of temperatures, ∼0.4 dex, compared to ∼0.2 dex for O VI and Ne VIII.

At $z = 0$, the column densities of O VI, Ne VI, and Ne VIII in AURIGA are higher than in APOSTLE at all radii, but the difference is maximal at the centre of the halo. Outside the central region, beyond ∼30 kpc, the differences in column density are fairly small, typically a factor of two or less. Although the mean column density differs at a given impact parameter, the range of column densities for the whole sample typically overlaps. The differences, however, can be substantial at higher redshift, $z \geq 1$. In Fig. 19, we see a general behaviour in the O VI, Ne VI, and Ne VIII profiles in both APOSTLE and AURIGA. In APOSTLE, the column density distributions are relatively flat, typically decreasing by only an order of magnitude over a radial range $3R_{200}$. In contrast, in AURIGA, the central column densities are typically higher and decrease much faster, dropping by over four orders of magnitude over the same radial range.

The differences in the column density profiles of O VI, Ne VI, and Ne VIII at $z \geq 1$ in APOSTLE and AURIGA are most notable in both the innermost and outermost regions. In AURIGA, the column densities of these ions are higher in the centre ($r < 50$ kpc), where they can be up to a hundred times higher than in APOSTLE. However, as the column densities in AURIGA decrease so rapidly with increasing radius, the column densities in APOSTLE end up being much higher in the outermost regions, ∼150 kpc. In particular, the column densities of these ions in the outer regions of APOSTLE are up to three orders of magnitude higher than in AURIGA. We also note that the column density variance at fixed impact parameter is much larger in AURIGA than in APOSTLE, particularly in the outer regions.

The ions O VII, O VIII, and Mg X probe some of the hottest gas surrounding our galaxies. O VII and O VIII probe a broad range of hot gas, $T \sim 10^{5.5}$–$10^{6.5}$ K and $T \sim 10^{6}$–$10^{6.5}$ K, respectively. Mg X probes gas in a narrower temperature range, $T \sim 10^{6}$–$10^{6.25}$ K. These three ions, O VII, O VIII, and Mg X, are shown in the fifth, sixth, and seventh rows from the top of Fig. 19. As with the other ions, we find fairly good agreement between APOSTLE and AURIGA at $z = 0$, with a considerable systematic offset for Mg X. Remarkably, the column densities of O VII and O VIII agree to within 10 per cent beyond the inner 10 kpc. Both APOSTLE and AURIGA predict relatively flat column densities as a function of impact parameter for both O VII and O VIII. The predictions for Mg X differ slightly. The column density of Mg X drops rapidly beyond radius ∼200 kpc and flattens to a near-constant value of $\sim 10^{12}$ cm^{-2} in both simulations. While the general shape of the profiles are similar in both simulations, the column density in APOSTLE is typically a factor of two to five higher than in AURIGA.

At $z \geq 1$, O VII, O VIII, and Mg X follow a similar trend as O VI, Ne VI, and Ne VIII. In the central regions, the column densities in AURIGA are either higher (O VII) or approximately equal to those in APOSTLE. Further out, the column densities are much higher in APOSTLE. This difference is due to the steeply declining column densities in AURIGA and the much flatter profiles in APOSTLE. The differences in O VII, O VIII, and Mg X between APOSTLE and AURIGA are most prominent at $z = 3$. Mg X is the most extreme case. In AURIGA it is only present within 40 kpc of the halo centre, whereas in APOSTLE there are still very high Mg X column densities out to 150 kpc and even beyond.

At the present day, the column densities of all the ions considered in Fig. 19 are broadly consistent in the two simulations within the halo-to-halo scatter. The main exception occurs in the central regions (≤30 kpc), where the AURIGA haloes typically have a peak in column density that can be up to a factor of 10 higher than in APOSTLE. These larger column densities at the centres of AURIGA haloes could be a signature of galactic fountains, which is where enriched, hot outflows recycle within a small central region. The other notable exception is the larger Mg X column density in APOSTLE, at all radii, but particularly in the outermost regions. This enhancement likely reflects the presence of more hot, $T \geq 10^6$ K, enriched gas at large radii in APOSTLE arising from the larger spatial extent of the hot outflowing material in this case.

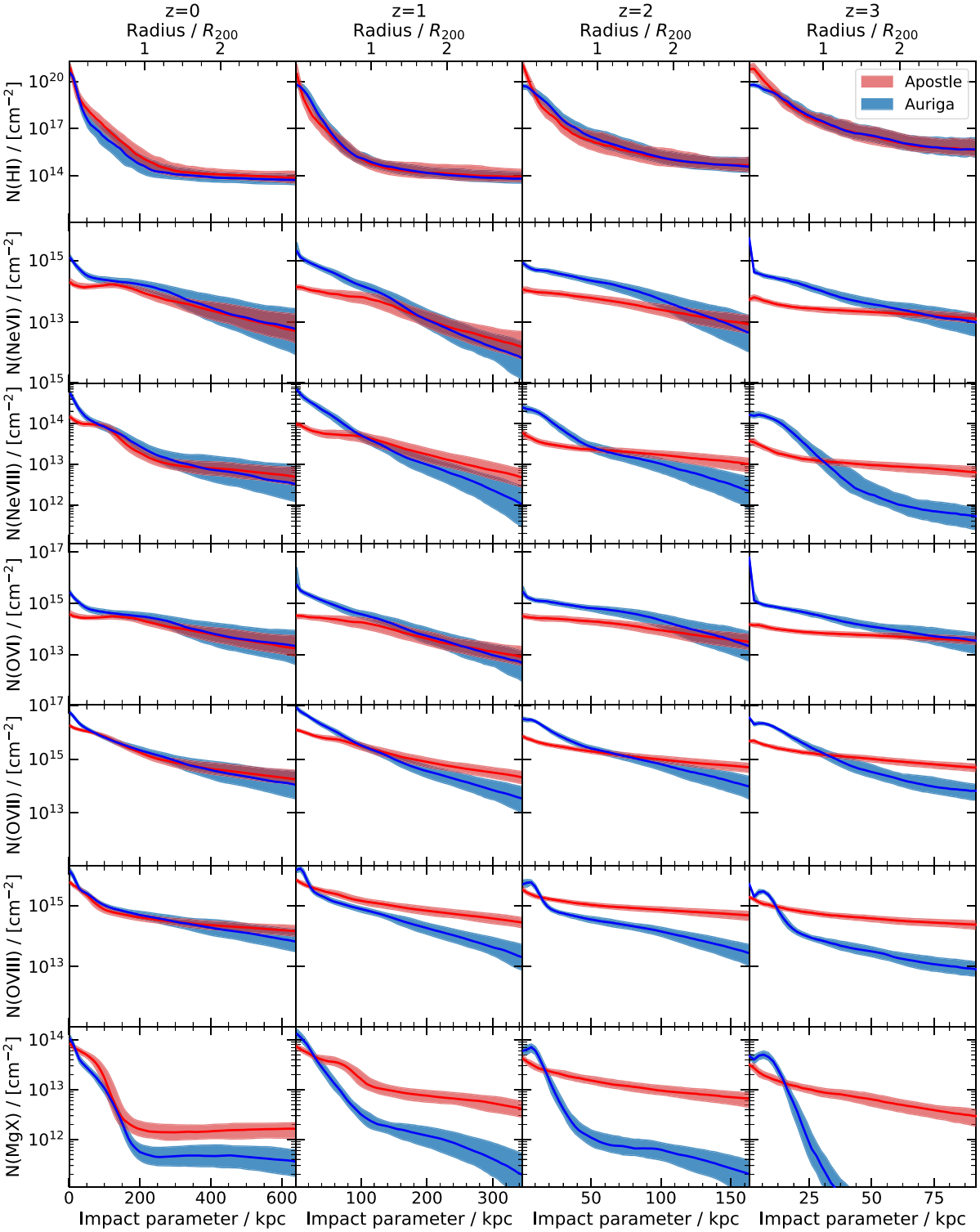

Figure 19. Atomic column number densities of several species as a function of impact parameter from the centre of the primary halo in both the APOSTLE (red) and AURIGA (blue) simulations, out to $3R_{200}$ at four redshifts $z \sim 0$, 1, 2, 3 from left to right, respectively. From top to bottom, the rows show results for H I, Ne VI, Ne VIII, O VI, O VII, O VIII, and Mg X, respectively. The column density at a fixed radius, r, for each halo is calculated by taking the median column density of many sightlines through a small annulus. We also compute the lower and upper quartiles of the column density in each annulus. The solid lines are the mean of the median column density, at each radius, for all four haloes. The shaded regions illustrate the range between the mean of the lower and upper quartiles for all of the haloes. We choose to use the median and quartiles as these are more comparable to a single random line of sight through a halo in the real universe. The results are binned by impact parameter, and the mean virial radius is used to show the approximate impact parameter as a function of R_{200} for all four haloes on the same plot.

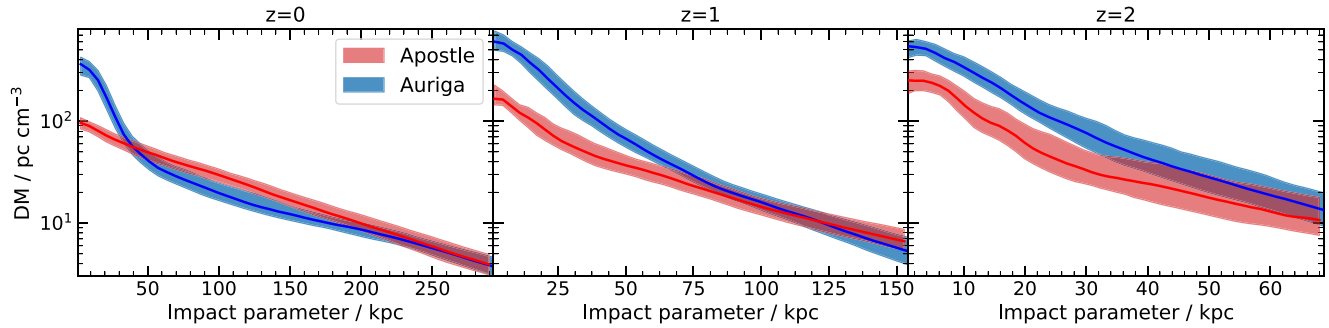

Figure 20. The dispersion measure of all four haloes in APOSTLE and AURIGA at three redshifts, $z \sim 0$, 1, 2 from left to right, respectively. The dispersion measure, at fixed radius, r, for each halo is calculated by taking the median dispersion measure of many sightlines through a small annulus of depth R_{200}. We also compute the lower and upper quartiles of the dispersion measure in each annulus. The solid line shows the mean of the median dispersion measure, at each radius, for all four haloes. The shaded region illustrates the range between the mean of the lower and upper quartiles for all the haloes. The dispersion measure at higher redshift is calculated in the frame of the halo at that redshift, not from an observer at the present day.

We find a consistent trend among all the ions considered in Fig. 19 for $z \geq 1$, with the exception of H I. This trend consists of higher column densities in the innermost regions of the AURIGA simulations, which then decline with impact parameter more rapidly than in APOSTLE. The important offshoot is that the APOSTLE haloes have significantly higher column densities at large radii, $\geq$100 kpc, with the differences increasing with redshift.

The large column densities of Ne VI, Ne VIII, O VII, O VIII, and Mg X in the outer regions of the APOSTLE simulations at $z \sim 1$–3 are a strong signature of hot, accretion-impeding outflows. A visual inspection of the evolving temperature projections in Fig. 9 demonstrates that hot gas, $T \sim 10^6$ K, in APOSTLE extends to radii of order $\geq 4R_{200}$ by $z = 3$. By contrast, the AURIGA galaxies develop a much cooler, $T \leq 10^{5.5}$, halo of gas which does not extend beyond $2R_{200}$. This hot gas distribution in AURIGA produces column densities that drop rapidly at $R_{200} \sim 50$ kpc at $z = 3$ and then drop even further beyond $3R_{200} \approx 150$ kpc.

The peak in the column densities of Ne VI, Ne VIII, O VI, O VII, and O VIII at the centre of the AURIGA haloes can be readily understood by reference to the density–temperature histograms in Fig. 15. Panels (a) and (b) show that there is a population of very dense gas, $n_H \geq 10^{-2}$ cm^{-3}, with temperatures in the range $T \approx 10^4$–10^7 K. As described in Section 6, this gas component appears to be a product of a galactic fountain. The high density of the gas leads to very short cooling times, ~200 Myr, so for such a massive gas component to be present it must be continuously replenished by the heating of dense gas. This gas is heated to $T \geq 10^6$ K where it cools at almost constant density before rejoining the ISM of the central galaxy. Therefore, the centrally concentrated peak in ion column densities in AURIGA appears to be a strong signature of galactic fountains.

In summary, we find that the APOSTLE simulations produce almost flat column density profiles for ions which probe hot gas, out to radii of $\sim 3R_{200}$ in the range $z = 0$–3. These flat density profiles are produced by hot, outflowing gas driven by SNe within the central galaxy. In contrast, the AURIGA simulations predict rapidly declining column densities with radius as the SNe-driven outflows are unable to eject large amounts of hot gas to such large radii. Instead, the AURIGA simulations generate galactic fountains where dense gas is heated to high temperatures, $T \approx 10^7$ K, and then cools at a high, almost constant, density. This fountain produces an observable central peak in the column densities of Ne VI, Ne VIII, O VI, O VII, and O VIII which is not present in APOSTLE.

7.2 Dispersion measure

The dispersion measure is a measure of the free electron column density along a sightline and, potentially, one of the most useful metrics of the baryon content of the Local Group. As discussed in Section 3.4, CHIME is predicted to detect between 2 and 40 FRBs d^{-1} over the whole sky (Connor et al. 2016). The hot halo of M31 makes a significant contribution to the dispersion measure of FRBs when their emission passes through the halo with an impact parameter of $\leq$150 kpc; this corresponds to an angle of approximately 11° on the sky, assuming that M31 is ~770 kpc away from the MW. Therefore, M31 covers ~400 deg^2, or ~ 1 per cent of the sky. This implies that the CHIME survey should expect to detect roughly between 10 and 150 FRB's per year behind the M31 halo. These can be compared with sightlines adjacent to M31. If the foreground contribution from the MW is uniform, or at least smooth over a narrow range of viewing angles, and the FRB population has the same redshift distribution over this range, the differences in these dispersion measures will be a direct reflection of the properties of the plasma in M31. The contribution of M31 to the dispersion measure can then be used to infer the amount of hot gas present in M31 and, thus, to constrain its baryon fraction.

In this section, we compute the dispersion measure from several thousand random sightlines through the four primary MW-like haloes at three redshifts, $z = 0$, 1, 2. The electron column density is calculated for parallel sightlines as described in Section 7.1. These are projected directly through $2 \times R_{200}$ of the primary halo at varying impact parameters. The dispersion measure at a given radius of each halo is calculated by taking the median of many sightlines in a small annulus. We project through the x, y, and z axes and combine the results. Additionally we compute the lower and upper quartiles in each annulus.

The dispersion measure profiles in Fig. 20 represent idealized observations of M31 from Earth, with contributions from the MW and material beyond M31 removed (i.e. the IGM and other distant haloes). In practice, we expect the contribution from halo gas in M31 to be large, and thus to be readily detectable when compared with sightlines that do not pass through M31. Although they are not realistic mocks of observations from Earth, the results in Fig. 20 provide some insight into how the dispersion measure of a halo varies with impact parameter and redshift, and thus may help interpret observational data. Later in this section, we discuss how future work could improve the realism of the simulated profiles and how

they could be used to exploit the constraining power of future observations.

With current data it is only possible to make direct measurements of today's dispersion measure around M31 and other Local Group galaxies. We do, however, include results from higher redshifts in Fig. 20 to understand how the dispersion measure evolves and to give insight on the possible background contributions to observations. (The dispersion measure at higher redshift is calculated in the frame of the halo at that redshift, not from an observer at the present day.)

At the present day, both simulations predict a similar trend, with the dispersion measure being highest in the central regions and declining with increasing impact parameter. At $z = 0$, the dispersion measure typically drops from a peak value of $\geq 10^2$ pc cm^{-3} in the centre of the halo to $\sim$1 pc cm^{-3} at R_{200}, and continues to fall beyond this radius (not shown in the figure). Beyond the inner 50 kpc, APOSTLE and AURIGA predict similar profiles. The main difference occurs in the centre of the halo. In APOSTLE the dispersion measure decreases with impact parameter at an almost constant rate. In AURIGA there is a peak at the very centre which drops rapidly out to 50 kpc. Beyond that, both the slope and amplitude of the profiles in the two simulations are approximately equal.

The peak in the dispersion measure in the inner regions of AURIGA is also present at higher redshifts. At $z \geq 1$ a similar peak, but of lower amplitude, also appears in the APOSTLE simulations. The peak at the centre of the AURIGA haloes at all redshifts coincides with the peak in the column densities of the ions that trace the warm–hot gas within the CGM (see Fig. 19) Thus, the origin of this large dispersion measure is plausibly the same as that of the ions. Feedback produces hot, metal-enriched, centrally concentrated gas which is dense. This gas then cools, at an almost constant density, before rejoining the ISM. The electron mass will trace the gas mass in Fig. 15(a). It is the hot gas of atomic density $\geq$0.001 cm^{-3} in AURIGA that produces the centrally concentrated dispersion measure peak. This gas is not present in APOSTLE at $z = 0$ and, as a result, the profile is much flatter near the centre.

At higher redshift, AURIGA predicts a higher dispersion measure throughout the halo. This behaviour is similar to that of the column densities of Ne VI, Ne VIII, O VI, and O VII in the central regions seen in Fig. 19, which typically probe gas at temperature $\sim 10^{5.5}$ K. The difference in baryon mass in the haloes of APOSTLE and AURIGA drives the difference in the amplitude of the dispersion measure profiles.

At lower redshift, the baryon fraction of the AURIGA haloes is still a factor of two higher than the APOSTLE counterparts. However, the dispersion measure in two simulations tends to agree reasonably well outside of the central region, $\geq$50 kpc. Inside the central region, the AURIGA haloes boast a significantly higher dispersion measure, thus indicating that the extra baryonic mass in AURIGA, at present day, is centrally concentrated. Efficient galactic fountains in AURIGA can continuously produce centrally concentrated hot gas.

In summary, the dispersion measure is a measure of the amount of ionized gas along the line of sight and is strongly sensitive to the distribution of hot gas around MW-mass haloes, which is mostly ionized. The similar dispersion measure profiles in the outer regions of APOSTLE and AURIGA at $z = 0$ imply that the haloes in the two simulations have similar amounts of hot gas in this region, despite having large differences in baryon fraction. This is possible as the extra baryons present in AURIGA are centrally concentrated due to the galactic fountains, which leads to a large central peak in the dispersion measure profile in AURIGA.

We predict that future surveys of dispersion measure inferred from FRBs should be able to identify or exclude the existence of a galactic fountain in either the MW or M31, through analysis of dispersion measure variation with impact parameter within the central regions. We also expect that the background, e.g. the contributions from the IGM and other intervening haloes at higher redshift, should be larger if there are hot, spatially extended outflows at high redshift, such as those found in APOSTLE. It may also be possible to identify the presence of a hot galactic fountain by direct observation of X-ray emission (Oppenheimer et al. 2020b).

In this analysis, we did not include material which is part of the ISM. When calculating the free electron density we discarded gaseous material with an atomic number density $\geq$0.1 cm^{-1} or a temperature $\leq 10^4$ K. Gas in this regime is not modelled explicitly in the simulations, however the distribution and morphology of the cold gas is in reasonable agreement with observations (Marinacci et al. 2017). The dispersion measure profiles in the innermost regions may well be higher than predicted in this work due to dispersion by ISM gas. However, predictions for the ISM suggest that it contributes only $\leq$50 pc cm^{-3} (Lorimer et al. 2007); thus the central regions should be dominated by contributions from halo gas.

Finally, we stress that realistic mock catalogues will be needed to interpret future data. Constructing these will require combining high-resolution Local Group simulations such as those presented here with large-volume cosmological simulations to determine the expected background.

7.3 Comparing to current observations

In this section, we compare our preliminary mock observations of the column densities of Ne VIII for our sample of four MW-mass haloes with current observations. The COS-Halos survey (Tumlinson et al. 2013) and CASBaH survey (Burchett et al. 2019) are absorption line studies of galaxies in the UV. They typically cover the redshift range $0.05 < z < 1.5$ and provide information on column densities and covering fractions of H I, Ne VIII, and O VI. Burchett et al. (2019) collated a statistical sample of Ne VIII CGM absorbers. This sample includes 29 CGM systems in the redshift range $z = 0.5$–1.5, with a median redshift, $z = 0.68$, stellar masses in the range $10^{9.5}$–$10^{11.5}$ M$_\odot$, and impact parameters within 450 kpc of the central galaxy.

In Fig. 21, we compare the column density of Ne VIII, as in Fig. 19, at $z = 0.5$ for both APOSTLE and AURIGA, with observational data, including both the detections (solid black circles) and non-detections (empty triangles) of Burchett et al. (2019). The highest inferred column density of Ne VIII is 14.98 ± 0.09 cm^{-2} at an impact parameter of 69 kpc and redshift, $z = 0.93$. The central galaxy of this system has an estimated stellar mass of $10^{11.2}$ M$_\odot$, slightly larger than our simulated galaxies. This high observed column density is larger than found in any of the predictions of APOSTLE and AURIGA, as seen in the figure. However, column densities this high are not uncommon at lower impact parameters in AURIGA.

The column densities at slightly larger radii, 100–200 kpc, are consistent with the predictions of both simulations, with almost all of the observational detections in this range overlapping the results from our simulations within the uncertainties. In the outer regions, the observations are dominated by upper limits which are higher than, and thus consistent with, the inferred column densities in the simulations.

The observations follow the general trend that the inner regions are dominated by detections of $\approx 10^{14}$ cm^{-2}, whereas the outer regions are mostly upper limits in the range $\approx 10^{13.5}$–10^{14} cm^{-2}. This is suggestive of a Ne VIII column density profile which typically declines by $\geq$0.5 dex between an impact parameter of 150 and 300 kpc. This is also seen in both APOSTLE and AURIGA. APOSTLE better recovers

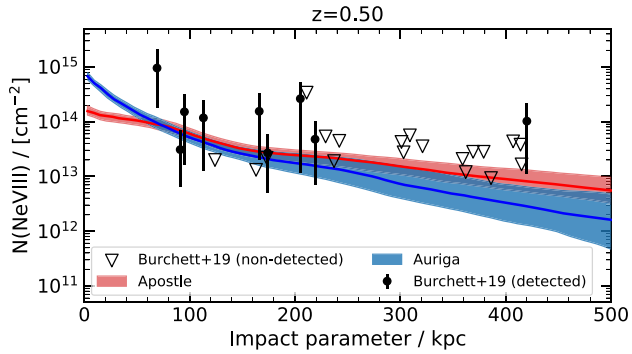

Figure 21. The atomic column number density of Ne VIII as a function of impact parameter from the centre of the primary halo in both the APOSTLE (red) and AURIGA (blue) simulations out to 500 kpc at $z = 0.5$. The column density at a fixed radius, r, for a single halo is calculated by taking the median column density of many sightlines through a small annulus. We also compute the lower and upper quartiles of the column density in each annulus. The solid line shows the mean of the median column density, at each radius, for all four haloes. The shaded region illustrates the range between the mean of the lower, and upper quartiles, for all of the haloes sampled. We also include the observational detections (solid black circles) and non-detections (empty triangles) of Burchett et al. (2019).

the (approximately) flat distribution of Ne VIII detections; however, AURIGA agrees better with the higher central column densities. In any case, the model preferences are driven by two data points, the ones with the lowest and highest impact parameters. Therefore, the model choice is subjective, and there is no clear preference towards either APOSTLE or AURIGA.

8 DISCUSSION AND CONCLUSIONS

The two simulations that we have analysed in this work have been shown to reproduce many galaxy observables even though they involve different galaxy formation models and hydrodynamical schemes. In particular the large-volume EAGLE simulations, which are similar APOSTLE simulations, reproduce the galaxy stellar mass function (Schaye et al. 2015), the evolution of galaxy masses (Furlong et al. 2015), sizes (Furlong et al. 2017), and colours (Trayford et al. 2015). Similarly, large-volume simulations with a similar model to AURIGA have successfully reproduced the scaling relations and evolution of galaxy sizes (Genel et al. 2018), the formation of realistic disc galaxies (Pillepich et al. 2018), the gas-phase mass–metallicity relation (Torrey et al. 2019), and the diversity of kinematic properties observed in the MW-type galaxies (Lovell et al. 2018).

In this work, we have analysed the emergent baryon cycle around two Local Group-like volumes centred around a pair of haloes similar to those of the MW and M31. We investigated how the baryon cycle differed when using the different subgrid models of the APOSTLE and AURIGA simulations. While these models are similar, they have significantly different implementations of SNe and AGNs feedback. APOSTLE injects all the energy from SNe in the form of a thermal energy 'dump', whereas AURIGA uses hydrodynamically decoupled 'wind' particles that carry mass, energy, momentum, and metals away from the ISM to lower density regions of the galactic halo.

In Section 4, we explored the effects of the different feedback implementations on baryonic evolution, particularly the baryon fraction, in and around the two primary haloes as a function of time. We found the minimum baryon fraction within a sphere around a primary APOSTLE galaxy to be ≈ 40 per cent of the cosmic baryon budget, which is approximately half the value found in AURIGA. Furthermore, the APOSTLE simulations exhibit a baryon deficiency of ≥ 10 per cent within a radius ≥ 1 Mpc (comoving) of the halo, extending to ≈ 2 Mpc at the present day. Thus, in APOSTLE, the Local Group is a baryon-deficient environment. Conversely, in the AURIGA simulations the baryon fraction is within 5 per cent of unity at all radii ≥ 0.5 Mpc (comoving), and at all redshifts. This difference in the baryon evolution is remarkable given that both simulations use the exact same ICs and produce central galaxies with relatively similar stellar properties. This is consistent with the findings of Mitchell & Schaye (2022) which show the gas mass, and thus density, of the CGM are more sensitive to the baryon cycle than is the case for the properties of the central galaxy.

In Section 5, we conducted a census of all the baryons expected to lie within R_{200} at the present day due to gravitational forces alone (which we called 'pre-destined'). In APOSTLE we found that ~ 35 per cent of the baryonic counterparts of the $z = 0$ dark matter halo particles inhabit the primary halo, whereas in AURIGA approximately 70 per cent do. Furthermore, in APOSTLE we found that almost half of the baryon counterparts of dark matter particles that are missing *never entered the halo*: they are 'impeded'. By contrast, in AURIGA almost 90 per cent of the absent baryons entered the halo before being ejected.

We also found that the physical extent of ejected and impeded baryons, in both APOSTLE and AURIGA, is such that there is baryonic mixing between the two primary haloes. This baryonic mass transfer, shown in Fig. 14, indicates that the presence of M31 may influence the evolution of the MW and vice versa (see Borrow et al. 2020).

The large 'impeded' gas component in APOSTLE is produced by halo-scale fast outflows with high covering fractions. The AURIGA simulations do not produce sufficiently large outflows to impede accretion significantly. However, SNe feedback in both APOSTLE and AURIGA inject a similar amount of energy per unit mass into the surrounding gas. Thus, the different fates of the energetic gas must result from the method of injecting the energy, or the subsequent evolution of the gas (followed with two different hydrodynamical scheme). We strongly suspect that it is the former that is responsible for the different outcomes, however, at later times, it is likely that there are effects from AGNs feedback too.

This differences in the SNe subgrid prescriptions in APOSTLE and AURIGA result in the post-SNe temperature of the gas in APOSTLE being much higher that in AURIGA and, crucially, greater than 10^7 K. Thus, in APOSTLE radiative cooling is inefficient and the gas expands adiabatically. This expansion produces hot, low-density parcels of gas which are buoyant and accelerate outwards through the halo (Bower et al. 2017). Conversely, in AURIGA the lower post-SNe temperature makes radiatively cooling more efficient and the gas cools rapidly, at almost constant density, and recycles on a short time-scale.

To summarize, we have found that the processes that regulate the rate of star formation in an MW-mass galaxy can be classified into two broad categories: ejective and preventative. The AURIGA simulations are dominated by ejective feedback with relatively short recycling times, regulating star formation without significantly reducing the halo baryon fraction. However, in APOSTLE feedback at high redshift ejects a large mass of gas beyond R_{200}. This gas has such a large covering fraction and outward pressure that it can suppress the cosmological accretion of gas. These findings are consistent with the results from the large-volume EAGLE simulations (Mitchell et al. 2020a,b) and the NIHAO simulations (Tollet et al. 2019) which all identify reduced cosmic gas accretion rates due to feedback

processes. Wright et al. (2020) also show that outflows from AGNs feedback are able to decrease the solid angle available for cosmological gas accretion, thus also suppressing further accretion. The FIRE simulations (Muratov et al. 2015) present some evidence that bursts of star formation at high redshift can suppress gas accretion into the *inner* halo; however, it is not clear if this suppression extends to R_{200} or low redshift. The FIRE simulations also produce (almost) baryonically closed MW-mass haloes (Hafen et al. 2019), thus more closely resembling those in AURIGA, than APOSTLE. These results highlight a fundamental difference in the outcome of the feedback processes in various subgrid implementations.

A caveat is that the stellar mass of the central galaxies in APOSTLE is typically a factor of two lower than in AURIGA. In principle, we could 'tune' the feedback parameters in APOSTLE to produce more massive galaxies in 10^{12} $M_\odot$ haloes and still end up with baryon-deficient haloes due to preventative feedback. Schaller et al. (2015) demonstrate that the 'weak SNe' EAGLE variant can produce MW-mass haloes with stellar masses consistent with the AURIGA galaxies, albeit with weaker feedback than used in AURIGA. Furthermore, Wright et al. (2020) show that the rate of gas accretion at R_{200} for the same 'weak SNe' simulation differs from the EAGLE reference model used in this work by less than 20 per cent. Thus, the EAGLE 'weak SNe' simulation produces AURIGA-mass galaxies, while still suppressing cosmological gas accretion as shown in this work.

While we suspect SNe feedback as the leading cause of differences in the baryon cycle around our simulated galaxies, there are other differences in the two simulations that could contribute. Namely, both simulations use different hydrodynamical solvers; however Schaller et al. (2015) and Hopkins et al. (2018) have demonstrated that the treatment of feedback is more significant in determining the outcome of simulations of this kind than the details of the hydrodynamics solver. APOSTLE and AURIGA also use different implementations of AGNs feedback. We find that the effect of AGNs on the baryon cycles analysed in this work is subdominant; however, previous studies show they can still have a significant effect on the CGM and even the central galaxy. While van de Voort et al. (2021) show the total gas mass within the virial radius of an MW-mass halo simulated with the AURIGA model both with and without AGNs feedback differs by only a few per cent, the inclusion of AGNs feedback decreases the $z = 0$ stellar mass by ~ 30 per cent. More recently, Irodotou et al. (2021) explicitly showed that the quasar and radio modes of the Auriga AGNs feedback model suppress star formation in the inner and outer parts of the galaxy through ejective and preventative feedback, respectively (see also fig. 17 of Grand et al. 2017). Davies et al. (2020) show that AGNs feedback can significantly reduce the baryon fractions of haloes of mass $\sim 10^{12}$ $M_\odot$. They show that the baryon fraction, at fixed halo mass, shows a strong anticorrelation with the black hole mass. Oppenheimer et al. (2020a) also demonstrate that AGNs feedback can significantly reduce the baryon fraction of MW-mass haloes to very low values, particularly those with black holes of mass $\geq 10^7$ $M_\odot$.

As previously described, the APOSTLE simulations use a modified version of the EAGLE reference model in which the AGNs feedback is effectively weaker. At the same time the higher gas mass resolution in APOSTLE can make the stellar feedback more efficient. As a result, the present-day black hole masses in the APOSTLE haloes are all $\leq 10^{6.8}$ $M_\odot$. This means the baryon cycle in these haloes is dominated by stellar feedback.

In Section 7, we investigated the observable signatures of strong, accretion-impeding outflows in APOSTLE and efficient galactic fountains in AURIGA. We concluded that the APOSTLE simulations produce almost flat column density profiles of ions which probe hot gas – Ne VI, Ne VIII, O VI, O VII, O VIII, and Mg X – out to radii $\sim 3R_{200}$ in the range $z = 0$–3. These flat profiles are a signature of hot, outflowing gas driven by SNe within the central galaxy. In contrast, the AURIGA simulations predict rapidly declining column densities with radius, as the SNe-driven outflows are unable to eject large amounts of hot gas to such large radii. We attempted to constrain the two subgrid models by comparing to the data on Ne VIII presented by Burchett et al. (2019). Unfortunately, these data are not constraining due to the small number of detections at very small and very large impact parameters.

We also investigated the dispersion measure, which probes the integrated free electron density along the line of sight. We found that the main difference between the dispersion measure profiles in AURIGA and APOSTLE is also at the very centre. In AURIGA, there is a peak at impact parameter $\leq$50 kpc, not found in APOSTLE. The dispersion measure is a promising observational diagnostic of the evolution of baryons around galaxies. A combination of high-resolution Local Group analogues, like those presented in this work, and large-volume cosmological simulations would facilitate the production of more realistic mock catalogues of FRBs. Large cosmological volumes allow modelling random sightlines out to the typical FRB redshifts, $z \sim 2$. These background contributions can be added to predictions from Local Group analogues to make realistic mocks of what would be seen from the Earth when looking, for example, in the direction of M31. These can be compared with real sightlines in the direction of M31 and just adjacent to it. As future surveys should detect hundreds of FRBs per year behind M31, these observations should be able to constrain models and shed light on the dominant processes involved in the galactic baryon cycle.

To conclude, we find that ejective and preventative feedback work in tandem to reduce the amount of gas within haloes in the APOSTLE galaxy formation model. In AURIGA, MW-mass galactic haloes are almost 'baryonically closed', as ejective feedback beyond R_{200} typically re-accretes and does not significantly impede further cosmic gas accretion. These results are consistent with the analysis of Wright et al. (2020) which found that baryonic feedback plays two roles in regulating the evolution of haloes by both directly removing gas from haloes, and suppressing gas inflow to haloes. Future observations of FRBs and CGM ion absorption should provide valuable data to compare and constrain different galaxy formation models. Dwarf galaxies may also provide a suitable laboratory for studying the baryon cycle. In particular, Fig. 2 shows there are significant differences in the stellar-mass/halo-mass relation of lower mass galaxies in the two models; these differences carry over into the baryon fraction of these objects. It is also likely that the size of the heated gas coronae around haloes within the Local Group will affect the number of star-free dark matter haloes, which are even less massive than dwarf galaxies, in the local environment (Benítez-Llambay et al. 2017; Sykes et al. 2019).

SOFTWARE CITATIONS

This paper used the following software packages:

(i) GADGET (Springel 2005)
(ii) AREPO (Springel 2010)
(iii) PYTHON (Van Rossum & Drake 2009), with the libraries:

(a) NUMPY (van der Walt, Colbert & Varoquaux 2011)
(b) SCIPY (Jones et al. 2001)
(c) H5PY (Collette 2013)
(d) MATPLOTLIB (Hunter 2007)
(e) NUMBA (Lam, Pitrou & Seibert 2015)
(f) UNYT (Goldbaum et al. 2018)

ACKNOWLEDGEMENTS

We thank Joop Schaye and Josh Borrow for discussions and comments, which significantly improved the manuscript. This work was supported by the Science and Technology Facilities Council (STFC) consolidated grant ST/P000541/1. AJK acknowledges an STFC studentship grant ST/S505365/1. CSF acknowledges support by the European Research Council (ERC) through Advanced Investigator grant DMIDAS (GA 786910). AF acknowledges support by a UKRI Future Leaders Fellowship (grant no MR/T042362/1) and Leverhulme Trust. RG acknowledges financial support from the Spanish Ministry of Science and Innovation (MICINN) through the Spanish State Research Agency, under the Severo Ochoa Program 2020-2023 (CEX2019-000920-S). This work used the DiRAC@Durham facility managed by the Institute for Computational Cosmology on behalf of the STFC DiRAC HPC Facility (www.dirac.ac.uk). The equipment was funded by BEIS capital funding via STFC capital grants ST/K00042X/1, ST/P002293/1, ST/R002371/1, and ST/S002502/1, Durham University and STFC operations grant ST/R000832/1. DiRAC is part of the National e-Infrastructure.

DATA AVAILABILITY

The data underlying this article will be shared on reasonable request to the corresponding author.

REFERENCES

Anderson M. E., Bregman J. N., 2010, ApJ, 714, 320
Baugh C. M., 2006, Rep. Prog. Phys., 69, 3101
Behroozi P. S., Wechsler R. H., Conroy C., 2013, ApJ, 770, 57
Benítez-Llambay A. et al., 2017, MNRAS, 465, 3913
Bird S., Vogelsberger M., Sijacki D., Zaldarriaga M., Springel V., Hernquist L., 2013, MNRAS, 429, 3341
Booth C. M., Schaye J., 2009, MNRAS, 398, 53
Borrow J., Anglés-Alcázar D., Davé R., 2020, MNRAS, 491, 6102
Bower R. G., Schaye J., Frenk C. S., Theuns T., Schaller M., Crain R. A., McAlpine S., 2017, MNRAS, 465, 32
Bregman J. N., Anderson M. E., Miller M. J., Hodges-Kluck E., Dai X., Li J.-T., Li Y., Qu Z., 2018, ApJ, 862, 3
Brooks A. M., Governato F., Quinn T., Brook C. B., Wadsley J., 2009, ApJ, 694, 396
Burchett J. N. et al., 2019, ApJ, 877, L20
Callingham T. M. et al., 2019, MNRAS, 484, 5453
Christensen C. R., Davé R., Brooks A., Quinn T., Shen S., 2018, ApJ, 867, 142
Collette A., 2013, Python and HDF5. O'Reilly, Sebastopol, CA
Connor L., Lin H.-H., Masui K., Oppermann N., Pen U.-L., Peterson J. B., Roman A., Sievers J., 2016, MNRAS, 460, 1054
Cordes J. M., Chatterjee S., 2019, ARA&A, 57, 417
Crain R. A. et al., 2009, MNRAS, 399, 1773
Crain R. A. et al., 2015, MNRAS, 450, 1937
Cullen L., Dehnen W., 2010, MNRAS, 408, 669
Dalla Vecchia C., Schaye J., 2008, MNRAS, 387, 1431
Dalla Vecchia C., Schaye J., 2012, MNRAS, 426, 140
Davies J. J., Crain R. A., McCarthy I. G., Oppenheimer B. D., Schaye J., Schaller M., McAlpine S., 2019, MNRAS, 485, 3783
Davies J. J., Crain R. A., Oppenheimer B. D., Schaye J., 2020, MNRAS, 491, 4462
Davies J. J., Crain R. A., Pontzen A., 2021, MNRAS, 501, 236
Davis M., Efstathiou G., Frenk C. S., White S. D. M., 1985, ApJ, 292, 371
DeFelippis D., Genel S., Bryan G. L., Fall S. M., 2017, ApJ, 841, 16
Dolag K., Borgani S., Murante G., Springel V., 2009, MNRAS, 399, 497
Faerman Y., Sternberg A., McKee C. F., 2017, ApJ, 835, 52
Fattahi A. et al., 2016, MNRAS, 457, 844
Ferland G. J. et al., 2013, Rev. Mex. Astron. Astrofis., 49, 137
Flynn C., Holmberg J., Portinari L., Fuchs B., Jahreiß H., 2006, MNRAS, 372, 1149
Ford A. B., Davé R., Oppenheimer B. D., Katz N., Kollmeier J. A., Thompson R., Weinberg D. H., 2014, MNRAS, 444, 1260
Frenk C. S., White S. D. M., Davis M., Efstathiou G., 1988, ApJ, 327, 507
Furlong M. et al., 2015, MNRAS, 450, 4486
Furlong M. et al., 2017, MNRAS, 465, 722
Genel S., Vogelsberger M., Nelson D., Sijacki D., Springel V., Hernquist L., 2013, MNRAS, 435, 1426
Genel S. et al., 2018, MNRAS, 474, 3976
Genel S. et al., 2019, ApJ, 871, 21
Gingold R. A., Monaghan J. J., 1977, MNRAS, 181, 375
Goldbaum N. J., ZuHone J. A., Turk M. J., Kowalik K., Rosen A. L., 2018, J. Open Source Softw., 3, 809
Grand R. J. J. et al., 2017, MNRAS, 467, 179
Grand R. J. J. et al., 2019, MNRAS, 490, 4786
Gupta A., Mathur S., Krongold Y., Nicastro F., Galeazzi M., 2012, ApJ, 756, L8
Gupta A., Mathur S., Galeazzi M., Krongold Y., 2014, Ap&SS, 352, 775
Haardt F., Madau P., 2012, ApJ, 746, 125
Hafen Z. et al., 2019, MNRAS, 488, 1248
Hafen Z. et al., 2020, MNRAS, 494, 3581
Hayward C. C., Torrey P., Springel V., Hernquist L., Vogelsberger M., 2014, MNRAS, 442, 1992
Henden N. A., Puchwein E., Shen S., Sijacki D., 2018, MNRAS, 479, 5385
Hopkins P. F., 2013, MNRAS, 428, 2840
Hopkins P. F. et al., 2018, MNRAS, 480, 800
Hou J., Lacey C. G., Frenk C. S., 2019, MNRAS, 486, 1691
Hummels C. B., Smith B. D., Silvia D. W., 2017, ApJ, 847, 59
Hunter J. D., 2007, Comput. Sci. Eng., 9, 90
Irodotou D. et al., 2022, MNRAS, in press
Jenkins A., 2010, MNRAS, 403, 1859
Jones E., Oliphant T., Peterson P. 2001, SciPy: Open Source Scientific Tools for Python. Available at: http://www.scipy.org/
Katz N., Gunn J. E., 1991, ApJ, 377, 365
Katz N., Hernquist L., Weinberg D. H., 1992, ApJ, 399, L109
Keller B. W., Wadsley J. W., Wang L., Kruijssen J. M. D., 2019, MNRAS, 482, 2244
Kelly A. J., Jenkins A., Frenk C. S., 2021, MNRAS, 502, 2934
Kereš D., Katz N., Weinberg D. H., Davé R., 2005, MNRAS, 363, 2
Kereš D., Vogelsberger M., Sijacki D., Springel V., Hernquist L., 2012, MNRAS, 425, 2027
Lacey C., Cole S., 1994, MNRAS, 271, 676
Lam S. K., Pitrou A., Seibert S., 2015, in Proceedings of the Second Workshop on the LLVM Compiler Infrastructure in HPC, LLVM '15. ACM, New York, p. 1
Larson R. B., 1974, MNRAS, 169, 229
Le Brun A. M. C., McCarthy I. G., Schaye J., Ponman T. J., 2014, MNRAS, 441, 1270
Li Y., Bregman J., 2017, ApJ, 849, 105
Licquia T. C., Newman J. A., 2015, ApJ, 806, 96
Lorimer D. R., Bailes M., McLaughlin M. A., Narkevic D. J., Crawford F., 2007, Science, 318, 777
Lovell M. R. et al., 2018, MNRAS, 481, 1950
Lucy L. B., 1977, AJ, 82, 1013
McMillan P. J., 2011, MNRAS, 414, 2446
McQuinn M., 2014, ApJ, 780, L33
Madau P., Dickinson M., 2014, ARA&A, 52, 415
Marinacci F., Grand R. J. J., Pakmor R., Springel V., Gómez F. A., Frenk C. S., White S. D. M., 2017, MNRAS, 466, 3859
Mathews W. G., Baker J. C., 1971, ApJ, 170, 241
Matthee J., Schaye J., Crain R. A., Schaller M., Bower R., Theuns T., 2017, MNRAS, 465, 2381
Miller M. J., Bregman J. N., 2015, ApJ, 800, 14
Mitchell P. D., Schaye J., 2022, MNRAS, 511, 2948
Mitchell P. D., Schaye J., Bower R. G., Crain R. A., 2020a, MNRAS, 494, 3971

Mitchell P. D., Schaye J., Bower R. G., 2020b, MNRAS, 497, 4495
Muratov A. L., Kereš D., Faucher-Giguère C.-A., Hopkins P. F., Quataert E., Murray N., 2015, MNRAS, 454, 2691
Navarro J. F., Benz W., 1991, ApJ, 380, 320
Navarro J. F., White S. D. M., 1993, MNRAS, 265, 271
Navarro J. F., White S. D. M., 1994, MNRAS, 267, 401
Navarro J. F., Frenk C. S., White S. D. M., 1995, MNRAS, 275, 720
Navarro J. F., Frenk C. S., White S. D. M., 1997, ApJ, 490, 493
Nelson D., Vogelsberger M., Genel S., Sijacki D., Kereš D., Springel V., Hernquist L., 2013, MNRAS, 429, 3353
Nelson D., Genel S., Vogelsberger M., Springel V., Sijacki D., Torrey P., Hernquist L., 2015, MNRAS, 448, 59
Nelson D. et al., 2018, MNRAS, 475, 624
Nelson D. et al., 2019, Comput. Astrophys. Cosmol., 6, 2
Oppenheimer B. D., Davé R., Kereš D., Fardal M., Katz N., Kollmeier J. A., Weinberg D. H., 2010, MNRAS, 406, 2325
Oppenheimer B. D. et al., 2020a, MNRAS, 491, 2939
Oppenheimer B. D. et al., 2020b, ApJ, 893, L24
Pearce F. R. et al., 1999, ApJ, 521, L99
Petroff E., 2017, preprint (arXiv:1709.02189)
Pillepich A. et al., 2017, MNRAS, 473, 4077
Pillepich A. et al., 2018, MNRAS, 475, 648
Planck Collaboration XI, 2013, A&A, 557, A52
Price D. J., 2008, J. Comput. Phys., 227, 10040
Price D. J., 2012, J. Comput. Phys., 231, 759
Rosas-Guevara Y. M. et al., 2015, MNRAS, 454, 1038
Sales L. V., Navarro J. F., Theuns T., Schaye J., White S. D. M., Frenk C. S., Crain R. A., Dalla Vecchia C., 2012, MNRAS, 423, 1544
Sawala T. et al., 2016, MNRAS, 457, 1931
Schaller M., Dalla Vecchia C., Schaye J., Bower R. G., Theuns T., Crain R. A., Furlong M., McCarthy I. G., 2015, MNRAS, 454, 2277
Schaye J., Dalla Vecchia C., 2008, MNRAS, 383, 1210
Schaye J. et al., 2010, MNRAS, 402, 1536
Schaye J. et al., 2015, MNRAS, 446, 521
Sérsic J. L., 1963, Boletin de la Asociacion Argentina de Astronomia La Plata Argentina, 6, 41
Shull J. M., Danforth C. W., 2018, ApJ, 852, L11
Sijacki D., Vogelsberger M., Kereš D., Springel V., Hernquist L., 2012, MNRAS, 424, 2999
Smith B. D. et al., 2016, Astrophysics Source Code Library, record ascl:1612.020
Smith M. C., Sijacki D., Shen S., 2018, MNRAS, 478, 302
Sokołowska A., Babul A., Mayer L., Shen S., Madau P., 2018, ApJ, 867, 73
Sommer-Larsen J., Gelato S., Vedel H., 1999, ApJ, 519, 501
Springel V., 2005, MNRAS, 364, 1105
Springel V., 2010, MNRAS, 401, 791
Springel V., Hernquist L., 2003, MNRAS, 339, 289
Springel V., White S. D. M., Tormen G., Kauffmann G., 2001, MNRAS, 328, 726
Suresh J., Nelson D., Genel S., Rubin K. H. R., Hernquist L., 2019, MNRAS, 483, 4040
Sykes C., Fumagalli M., Cooke R., Theuns T., Benítez-Llambay A., 2019, MNRAS, 487, 609
Thacker R. J., Couchman H. M. P., 2001, ApJ, 555, L17
Tollet É., Cattaneo A., Macciò A. V., Dutton A. A., Kang X., 2019, MNRAS, 485, 2511
Torrey P., Vogelsberger M., Sijacki D., Springel V., Hernquist L., 2012, MNRAS, 427, 2224
Torrey P., Vogelsberger M., Genel S., Sijacki D., Springel V., Hernquist L., 2014, MNRAS, 438, 1985
Torrey P. et al., 2019, MNRAS, 484, 5587
Trayford J. W. et al., 2015, MNRAS, 452, 2879
Tumlinson J. et al., 2013, ApJ, 777, 59
van de Voort F., Schaye J., Booth C. M., Haas M. R., Dalla Vecchia C., 2011a, MNRAS, 414, 2458
van de Voort F., Schaye J., Booth C. M., Dalla Vecchia C., 2011b, MNRAS, 415, 2782
van de Voort F., Bieri R., Pakmor R., Gómez F. A., Grand R. J. J., Marinacci F., 2021, MNRAS, 501, 4888
van der Walt S., Colbert S. C., Varoquaux G., 2011, Comput. Sci. Eng., 13, 22
Van Rossum G., Drake F. L., 2009, Python 3 Reference Manual. CreateSpace, Scotts Valley, CA
Vogelsberger M., Sijacki D., Kereš D., Springel V., Hernquist L., 2012, MNRAS, 425, 3024
Vogelsberger M., Genel S., Sijacki D., Torrey P., Springel V., Hernquist L., 2013, MNRAS, 436, 3031
Vogelsberger M. et al., 2014, MNRAS, 444, 1518
White S. D. M., Frenk C. S., 1991, ApJ, 379, 52
White S. D. M., Rees M. J., 1978, MNRAS, 183, 341
Wiersma R. P. C., Schaye J., Smith B. D., 2009a, MNRAS, 393, 99
Wiersma R. P. C., Schaye J., Theuns T., Dalla Vecchia C., Tornatore L., 2009b, MNRAS, 399, 574
Wijers N. A., Schaye J., Oppenheimer B. D., Crain R. A., Nicastro F., 2019, MNRAS, 488, 2947
Wijers N. A., Schaye J., Oppenheimer B. D., 2020, MNRAS, 498, 574
Wright R. J., Lagos C. d. P., Power C., Mitchell P. D., 2020, MNRAS, 498, 1668
Zheng Z., Ofek E. O., Kulkarni S. R., Neill J. D., Juric M., 2014, ApJ, 797, 71

APPENDIX A: STELLAR DISC PROPERTIES

Fig. A1 shows stellar surface density profiles, for stellar mass within ± 5 kpc of the mid plane in the vertical direction, for all simulations at $z = 0$. The profiles are simultaneously fit with a linear sum of an exponential profile of scale radius, $R_{\rm D}$, and a Sersic profile of the form $\exp{(R/R_{\rm eff})^n}$ (Sérsic 1963). The best-fitting values are calculated using the least squares method to logarithm density profile.

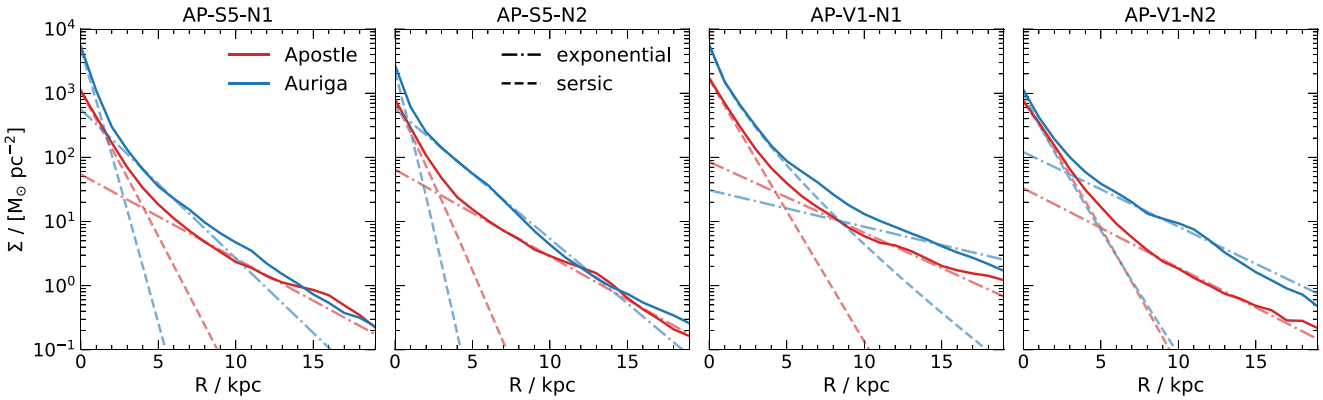

Figure A1. The radial stellar surface density profiles of the four primary haloes. The surface densities are calculated using all the stellar particles within a physical height of ±5 kpc from the galactic plane; these are shown as solid lines. The radial profiles are simultaneously fit with a Sersic (dashed) and exponential (dash–dotted) profile using a non-linear least-squares method. Results for the APOSTLE and AURIGA simulations are shown in red and blue, respectively. The best-fitting parameters may be found in Table 1.

This paper has been typeset from a TEX/LATEX file prepared by the author.